



Development of a Stress Transfer Function for an Idealised Helicopter Structure

Frank G. Polanco

DSTO-RR-0171

Development of a Stress Transfer Function for an Idealised Helicopter Structure

Frank G. Polanco

**Airframes and Engines Division
Aeronautical and Maritime Research Laboratory**

DSTO-RR-0171

ABSTRACT

This report presents an investigation of the effects that may have an influence on the development of a linear stress transfer function (STF) relating the stress in dynamic components to the stress in static components. Effects such as buckling, non-uniqueness, vibration, and solution procedure are considered. Two procedures for determining the STF are compared, one termed the vector procedure and the other the matrix procedure. A simple two dimensional truss, which models an idealised helicopter structure, is constructed to numerically simulate the development of a STF. Using random inputs the resulting stresses are evaluated exactly. Noise is then added to both the input loads and output stresses to develop a noisy data set. Using this noisy data set, STFs are developed using both the vector and matrix techniques. The vector procedure is shown to be sensitive to collinearity in the input, while the matrix technique is found to be more stable under the same ill-conditioning.

RELEASE LIMITATION

Approved for public release

DEPARTMENT OF DEFENCE
DEFENCE SCIENCE & TECHNOLOGY ORGANISATION

DSTO

Published by

*DSTO Aeronautical and Maritime Research Laboratory
PO Box 4331
Melbourne Victoria 3001 Australia*

*Telephone: (03) 9626 7000
Fax: (03) 9626 7999
© Commonwealth of Australia 2000
AR-011-237
March 2000*

APPROVED FOR PUBLIC RELEASE

Development of a Stress Transfer Function for an Idealised Helicopter Structure

Executive Summary

At present, helicopter component fatigue estimates are necessarily conservative to take account of the large variability in component load under the same flight condition. This means that most components could still be safely used past their component retirement times. However, one researcher has found that the level of conservatism applied may not always be adequate, and that the retirement lives of a few components may need to be reduced by as much as 75%. Hence, some components may remain in service for periods in excess of their safe fatigue lives. An accurate history of component loads would fulfil two seemingly contradictory objectives, increasing safety while reducing costs.

However, due to a harsh working environment, strain measuring devices placed directly on dynamic components have a limited life span. In addition, the information transmitted (either via slip-rings or telemetry) from these *in situ* devices is often unreliable. Hence we developed a linear stress transfer function (STF) that relates the stress in a dynamic component to the stresses in static components. An investigation of STF development was undertaken using an idealisation of a helicopter's structure.

Potential applications of this work include:

- the accurate determination of component fatigue life expended (with component retirement life implications),
- the parallel development of a health monitoring system (using redundant information from the STF), and
- a real-time system warning pilots of excessive aircraft loads.

Authors

Frank G. Polanco

Airframes and Engines Division

Frank Polanco graduated in 1992 with a Bachelor of Aerospace Engineering (Honours) and a Bachelor of Applied Science (Distinction) from the Royal Melbourne Institute of Technology (RMIT). He joined the Aeronautical and Maritime Research Laboratory (AMRL) in 1993, working on aircraft structural integrity and fatigue life monitoring before returning to RMIT to complete a Doctorate in Mathematics. He then rejoined the AMRL in 1998 to work in the area of helicopter life assessment.

Contents

1. INTRODUCTION.....	1
2. TRUSS MODEL	4
2.1 Simple Truss Model.....	4
2.2 Introduction of Non-linearity.....	5
2.3 Problems with Uniqueness.....	6
2.4 Stress Estimation with Known External Load.....	8
2.5 Stress Estimation with Unknown External Load.....	11
3. NUMERICAL EXAMPLE OF A 2-D HELICOPTER TRUSS	12
3.1 Noiseless Stress Estimations	13
3.2 Noisy Stress Estimations with Known External Load (matrix technique)	15
3.3 Noisy Stress Estimations with Unknown External Loads (vector technique)	22
4. PRELIMINARY RESULTS OF A SIMPLIFIED TRUSS	26
5. DISCUSSION	31
6. CONCLUSION.....	33
7. REFERENCES	34
A. STATICALLY INDETERMINATE STRUCTURES REMAIN LINEAR	37
B. SOLUTION OF A 2-D STATICALLY DETERMINATE HELICOPTER TRUSS.....	39
B.1 Main Rotor Loads on Cabin Section.....	40
B.2 Accelerations on Cabin Section	41
B.3 Tail Loads	42
B.4 Stresses at Strain Gauge Locations.....	44
C. EFFECT OF VIBRATION ON STATIC ASSUMPTION.....	47
D. LEAST SQUARES SOLUTIONS	55
D.1 Singular Value Decomposition.....	55
D.2 Column Weighting.....	57
E. MAXIMUM ERROR OF AN APPROXIMATE MATRIX	59
E.1 Regions of Maximum Error	63

1. Introduction

Helicopter fatigue damage estimates are necessarily over-conservative at present, and do not account for variations in usage on an aircraft-to-aircraft basis. This can result in maintenance intervals that are shorter than necessary and the premature replacement of some components [1]. As Gunsallus and Robeson [2] correctly point out, *'[t]he user is constantly pushing the envelope of safe operation in efforts to extract the most safe usage from a given airframe'*. This explains the emphasis on improving the estimation of helicopter fatigue damage [3–17].

Helicopters, unlike fixed-wing aircraft, usually have single (non-redundant) load paths and are subjected to both high cycle and low cycle fatigue loads [18]. The fatigue life of a helicopter component is clearly dependent on the loading history experienced by that component, but the manufacturer's fatigue life estimation is based on a predicted usage spectrum [1, 19–25]. However, the usage spectrum experienced by helicopters is normally different to that envisaged by the operator and the manufacturer before the aircraft enters service. This varied usage spectrum, together with the fact that the severity of individual manoeuvres varies widely both between pilots and between individual helicopters [26, 27], imply that the fatigue lives of helicopter components are necessarily overly conservative in nature. An accurate estimation of loads in critical components would have two seemingly contradictory benefits—improved safety and reduced component replacement costs. There are possibly two added bonuses of installing an effective on-line load detection system. The first is a real-time warning system that could alert the pilot that a high fatigue manoeuvre is being entered, thus allowing the incidence of damaging loads to be reduced [28]. The second is a fault warning capability (either real-time or off-line), which could be implemented using redundant information from the developed system.

Currently, after every flight, the helicopter aircrew of the Australian Defence Force has to complete an EE360 Fatigue Monitoring Form, which documents rudimentary and easily quantifiable data on manoeuvres etc. For example, the information recorded on EE360 forms includes the number of landings, type of landing surface, percentage of time at high and low altitudes, and stores configuration. As expected, only simple fatigue calculations can be performed using EE360 data.

Barndt and Moon [19, p. 1375] state that installing a Structural Data Recording Set (SDRS) system *'translates into millions of dollars saved even after the installed system costs are considered'* and that a SDRS system would help *'identify aircraft exposed to severe operating conditions'*. Fatigue life estimates based on regime recognition provide an improvement when compared to those based solely on usage hours, but they still do not fully account for the actual variation of loads during a given manoeuvre [29].

The next level of complexity involves measuring stresses directly on critical structural components, which are mostly from the rotor system for helicopters. (For example, of

the 21 most fatigue-critical components on the AH-64A Apache, Lombardo [25, p. 46] states that 20 are from the rotor system.) However, slip rings or rotating telemetry required for such direct measurements of stress lack the reliability and maintainability needed for everyday fleet usage [29]. This constraint forces us to seek an alternative approach, such as developing a stress transfer function that relates stresses experienced by rotor system components to stresses measured in fixed components.

A companion report [30] surveys published research on helicopter fatigue estimation techniques. However, there appears to be a lack of elementary research into the underlying structure of this estimation problem. For example, several papers tackle the problem of non-orthogonal inputs using trial-and-error. Although somewhat effective, these procedures may not lend themselves to generalisations, especially when different helicopter types are considered. In this report, we investigate some of the more fundamental questions concerning the development of a stress transfer function. Although the development is not exhaustive, the findings do highlight some interesting properties about the underlying structure of the problem.

Throughout this report we assume the outputs from strain gauges have been converted to stresses. As such we use strain gauge output and stress interchangeably. We investigate aspects that influence the development of stress transfer functions between strain gauge outputs in static components. (We envisage that in the future this work will be expanded to include dynamic effects.) The effects investigated in developing transfer functions include, non-linearities (in particular those due to buckling), non-uniqueness (for example, rotor blade stress distribution), and solution procedure (how loading information affects results).

A simplified statically determinate helicopter structure is developed to examine alternative techniques of setting up the transfer functions. The difference between these techniques is whether the externally applied loads are known or unknown, and due to the nature of the solutions we term them *matrix* and *vector* techniques respectively. Either technique may be used for rotor component stress estimation, however, the matrix technique requires knowledge of external loading for the development of the transfer functions. Once the transfer functions are developed, neither technique requires external loading information. When the stress measuring systems contain no noise the two techniques give rise to identical solutions. However, initial results suggest that the matrix solution technique is more robust when the underlying system of equations is ill-conditioned. In fact, when the condition number (a measure of sensitivity) of the underlying system of equations is large, the vector solution technique may be unusable even for small amounts of noise in the stress measurement system.

The appendices present the investigation of a number of problems that arose along the way. Appendix A shows that indeterminate systems are still linear. In Appendix B we analytically solve for the stress at eight locations in a simplified helicopter truss. The truss is two-dimensional and statically determinate. Appendix C examines the effect of a static assumption on a dynamically-loaded simply-supported beam. Conditions

under which the static assumption remains valid are stated. Appendix D gives a brief overview of the least squares solution from a singular value decomposition perspective. Finally, Appendix E proves that the error surface (as defined) between a matrix and its approximation has only two maxima and two minima.

Applications of this work include:

- determining the fraction of fatigue life expended by components,
- a health monitoring system (for example, a system which detects cracks), and
- a real-time warning system of excessive loads.

2. Truss Model

By developing a simple two-dimensional analytic model in this section we can readily gain information about what problems may arise in more complex models (including the actual helicopter).

2.1 Simple Truss Model

We first consider the highly simplified truss model shown in Figure 2.1 for a generic helicopter. The striped sections above the main and tail rotors represent loading, m_{AD} and m_{AC} are point masses, G_i for $i=0,1,2,\dots,7$ denote strain gauges, P_x , P_y , and P_m are the main rotor loads, and T_x , T_y , and T_m are the tail rotor loads. All members are pinned together except for the vertical member connected to the main rotor, which passes through a slide bearing. The point masses allow forces due to accelerations (gravity for example) to be simulated.

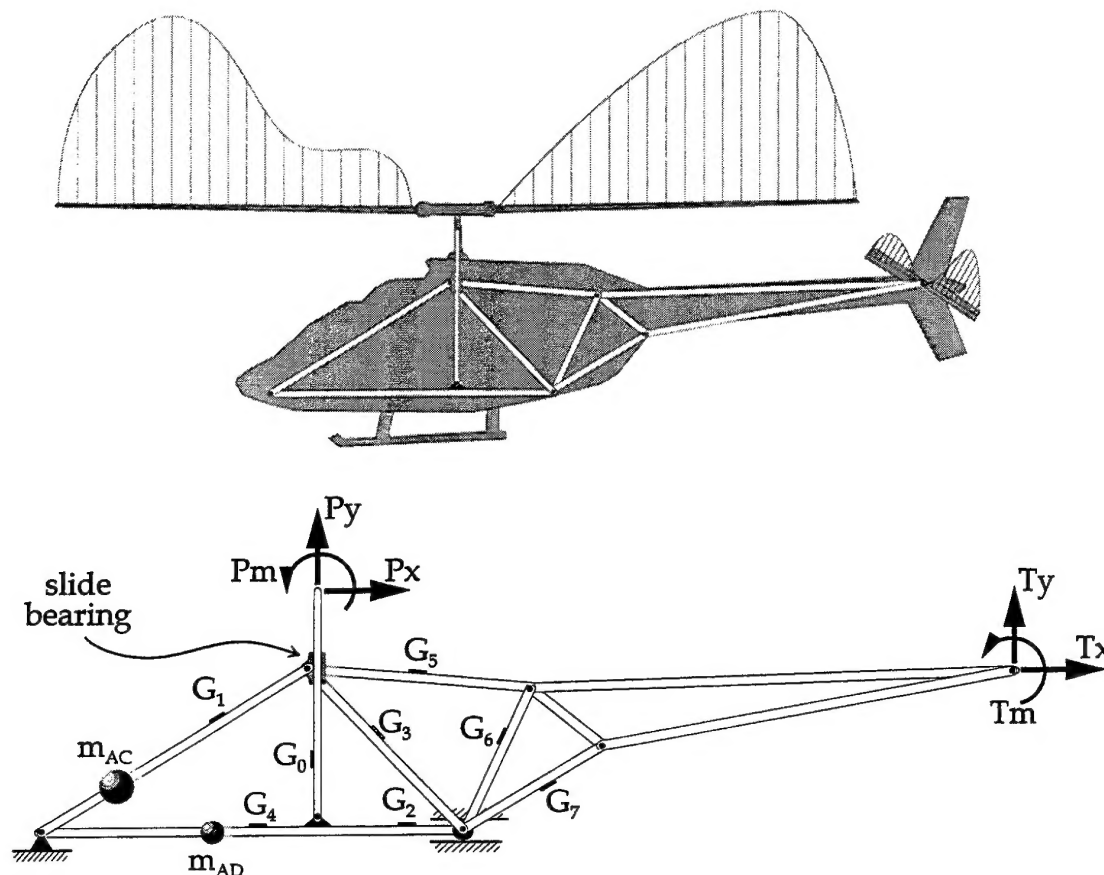


Figure 2.1. Simple two-dimensional truss model of a helicopter.

As can be seen from Figure 2.1 all main rotor system loads are transferred into the fuselage via the main rotor shaft (we will see in § 2.3 that this causes uniqueness problems when determining blade stresses from fuselage stresses). The tail rotor may be idealised in the same way. For simplicity we configured the problem to be a static one by pinning the bottom left joint to the ground and adding a roller to the bottom right joint (located to the right of gauge G_2). Appendix A shows two sets of examples demonstrating why indeterminate systems, although more complicated, may be treated using the same linear principles. The solution for the statically determinate truss shown in Figure 2.1 is given in Appendix B. Vibration effects in relation to the static assumption are discussed in Appendix C, where we show that under suitable conditions the static assumption yields a good approximation.

2.2 Introduction of Non-linearity

One way that the simple truss shown in Figure 2.1 could become non-linear is if one of the components were to buckle. (On an actual helicopter the skin is an example of a component subject to buckling.) Consider the rectangular shear panel, shown in both unbuckled and buckled states, in Figure 2.2 (figure after Brunh [31, p. C11.8] and in Timoshenko and Gere [32, p. 421]). We will consider what effects skin buckling has on the supporting stiffeners.

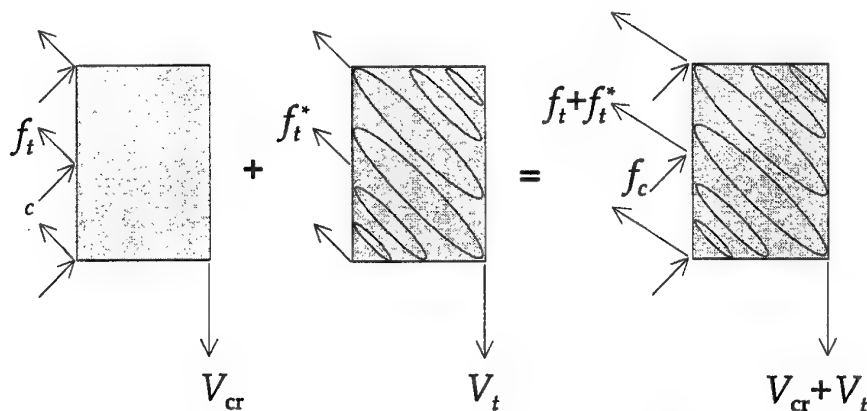


Figure 2.2. Buckled shear panel with ellipses depicting wrinkling. The shear panel has a bi-linear stress response to the vertical load, linear both before and after buckling.

The stresses on the left side of the panels, f_c and f_t , represent compressive and tensile stresses respectively. The shear panel on the left, under the critical load V_{cr} , is in a state just prior to buckling. The shear panel on the right, under a load $V_{cr} + V_t$, has buckled showing the characteristic wrinkling (depicted as ellipses). After buckling, the shear panel on the right may be thought of as being composed of two shear panels: one panel just before buckling (left panel) that can take compression, and another panel that can

act only as a tension field (middle panel). As can readily be seen any stress reading taken as a function of vertical load would result in a continuous bi-linear function with different slopes before and after buckling. Before buckling the panel would linearly take both compression and tension. After a critical load V_{cr} however, the panel would continue to take only tensile load. More precisely, the stress in the connecting stiffener would be of the form

$$\sigma = \begin{cases} c_1 V, & V \leq V_{cr} \\ c_2 + c_3 V, & V \geq V_{cr} \end{cases}$$

where V is the vertical load and c_1 , c_2 , and c_3 are constants which depend on the shear panel and stiffener properties (such as stiffness, area, and length) and on the angle which the wrinkles make with the horizontal. (See Bruhn [31, §C11.5] for further details.)

This type of non-linearity applies to local buckling as well, for example the flanges of a beam. Thus the stress within the beam will exhibit a bi-linear response to the applied load if the flange buckles during loading. These non-linear effects need to be taken into account in an implementation of this stress correlation method, and thus gauges should be placed away from buckling structures to achieve a linear relationship between measured stresses.

2.3 Problems with Uniqueness

Consider the truss shown in Figure 2.3 under two loads F_1 and F_2 at a distance x_1 and x_2 from the left end of the beam respectively (the shaded beam has length L).

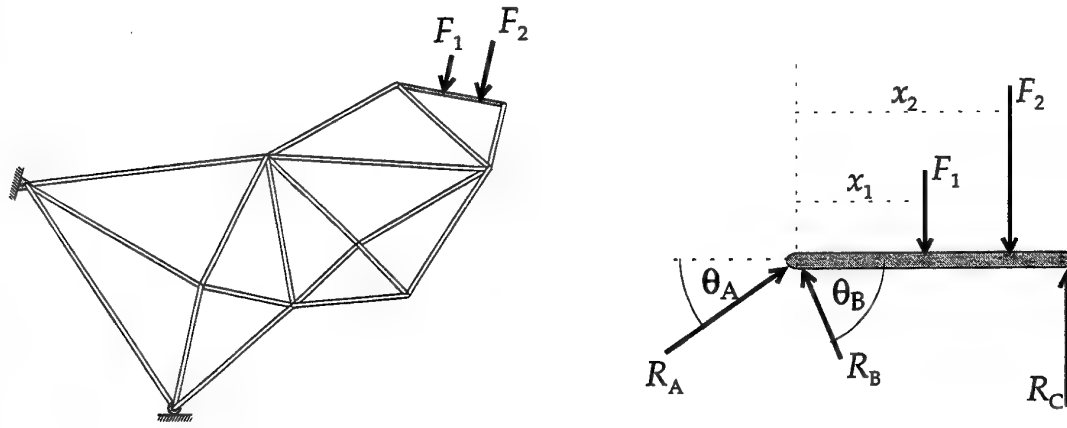


Figure 2.3. A non-unique loading configuration.

Solving for the reaction forces R_A , R_B , and R_C on the shaded beam gives

$$\begin{aligned}
 R_A &= R_B \frac{\cos \theta_B}{\cos \theta_A}, \\
 R_B &= \frac{\cos \theta_A}{\sin(\theta_A + \theta_B)} (\beta - \alpha), \quad \text{and} \\
 R_C &= \alpha,
 \end{aligned}$$

where $\alpha = F_1(x_1/L) + F_2(x_2/L)$ and $\beta = F_1 + F_2$. Thus the reaction forces are only a function of α and β . So that for any combination of constants α and β the reactions are also constant, despite the fact that both the loads and where they are applied may be varying. For example, if $L=1$ then the combination $F_1=3$, $F_2=7$, $x_1=0.3$, and $x_2=0.5$ gives the same stress distribution as the combination $F_1=18$, $F_2=-8$, $x_1=0.6$, and $x_2=0.8$ everywhere on the truss except in the shaded beam. There is no unique way to determine the stress in the shaded beam from the stress in the remainder of the truss using static information alone.

The same non-uniqueness problem arises when the blade loads are transferred through the main rotor mast onto the underlying structure. Figure 2.4 shows two different loading distributions on a single blade that produce the same vertical shear force and bending moment at the hub. (If the blade has unit length then the two bending moment distributions shown in Figure 2.4 are given approximately by $5.486 - 8.869x + 2.5x^2 - 1.647x^3 + 3.839x^4 - 1.310x^5$ and $5.486 - 8.869x - 34.05x^2 + 95.51x^3 - 80.82x^4 + 22.74x^5$. Differentiating the bending moment once gives the vertical shear force and differentiating twice gives the loading.) As can be seen from Figure 2.4, from statics alone there is no way to determine what the blade stress distribution is from the structure below the main rotor hub, since the shear and bending moment are identical at the hub.

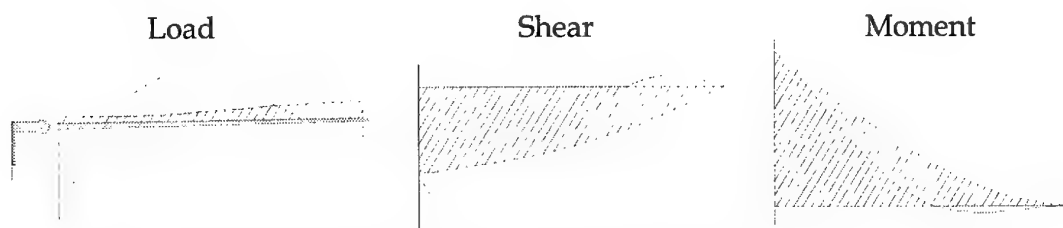


Figure 2.4. The hub sees the same shear and bending moment for two different loading distributions.

It is easy to prove that there is an infinite number of loading distributions that will give rise to any single combination of shear and bending moment. Let the bending moment distribution be given by

$$M(x) = \alpha + \beta x + f(x),$$

where α and β are constants, and $f(x)$ is any function that satisfies the two conditions $f(0) = f'(0) = 0$. Since shear, V , and the loading distribution, F , are simply given by the first and second derivatives of bending moment respectively, we have that

$$V(x) = \beta + f'(x),$$

and

$$F(x) = f''(x).$$

Thus the bending moment and shear at the origin will always be $M(0) = \alpha$ and $V(0) = \beta$ respectively, regardless of the function $f(x)$ chosen (provided it and its first derivative are zero at the origin).

Although in theory there is an infinite number of functions that satisfy the same bending and shear values at the root, in practice a vast majority of these loading distributions would never be realised. However, there are still a sufficiently large number of possible load combinations to yield a difficult non-uniqueness problem.

2.4 Stress Estimation with Known External Load

In the remainder of this report we assume all structures are static, that is, we ignore all dynamic effects. Define a *load* as any input having an influence on stress so that, for example, shearing forces (such as P_x), bending moments (such as T_m), and accelerations (such as g_x) are defined as loads. If we know both the loading and resulting stress on our simple helicopter truss we can write down the relation for the stress at the location of the k th strain gauge as a function of load

$$\sigma_k(t) = a_{1k}f_1(t) + a_{2k}f_2(t) + \dots + a_{Jk}f_J(t), \quad (2.1)$$

where the a_{jk} are constants (the subscripts j and k refer to the load and stress respectively), J is the number of input loads, and f_j is the j th load. (We have implicitly assumed that stress is a linear function of input loads.) Introduce a bracketed superscript notation for time so that $\sigma_k^{(i)} = \sigma_k(t_i)$, and apply a similar notation for the loading parameters. We can then write a linear system of equations that relate stress to loading as

$$\begin{matrix} \begin{bmatrix} \sigma_1^{(1)} & \sigma_2^{(1)} & \dots & \sigma_K^{(1)} \\ \sigma_1^{(2)} & \sigma_2^{(2)} & \dots & \sigma_K^{(2)} \\ \vdots & \vdots & \ddots & \vdots \\ \sigma_1^{(I)} & \sigma_2^{(I)} & \dots & \sigma_K^{(I)} \end{bmatrix} & = & \begin{bmatrix} f_1^{(1)} & f_2^{(1)} & \dots & f_J^{(1)} \\ f_1^{(2)} & f_2^{(2)} & \dots & f_J^{(2)} \\ \vdots & \vdots & \ddots & \vdots \\ f_1^{(I)} & f_2^{(I)} & \dots & f_J^{(I)} \end{bmatrix} & \begin{bmatrix} a_{11} & a_{12} & \dots & a_{1K} \\ a_{21} & a_{22} & \dots & a_{2K} \\ \vdots & \vdots & \ddots & \vdots \\ a_{J1} & a_{J2} & \dots & a_{JK} \end{bmatrix} \\ I \times K & & I \times J & J \times K \end{matrix},$$

where I is the number of observations (of load and stress taken at different times) and K is the number of strain gauges.

For ease of description let's consider a single strain gauge, that is $K = 1$. In this case the system of equations is over-determined if $I > J$ (there are more observations I than unknowns J) and under-determined if $I < J$ (there are more unknowns than observations). In practice the under-determined system would not arise if an arbitrary number of observations were possible, and hence will not be discussed below.

If the system has full rank (that is, the force matrix has linearly independent rows) and there are as many observation as loads ($I = J$) then we can easily find the coefficient matrix. The product of the inverted force matrix by the stress matrix gives the coefficient matrix

$$[A] = [F]^{-1} [\Sigma],$$

where $[A]$ is the force coefficient matrix, $[F]$ is the force matrix, and $[\Sigma]$ is the stress matrix. However, if we were to have the luxury of being able to choose the force matrix to be the identity matrix, then the coefficient matrix would be identical to the stress matrix.

If the system has full rank and is over-determined ($I > J$), then there is no unique solution. A unique solution is obtained by minimising the norm of the residual, where the residual is defined as $[F][A] - [\Sigma]$. Minimising over the 2-norm gives rise to the least squares (LS) problem. Golub and van Loan [33] suggest either the method of normal equations or QR factorisation for the solution of the LS problems. The method of normal equations involves computing the Cholesky factorisation of the product of the force matrix transpose and the force matrix. The accuracy of this method's solution depends on the square of the condition number κ , which for the 2-norm is defined as the ratio of the largest to smallest singular values of the force matrix (see Appendix D.1 for a discussion of singular values). The QR factorisation's LS solution involves obtaining the Householder QR factorisation of the loads matrix and using the result in the solution of an equivalent, but easier to solve, LS problem. The QR factorisation method runs into trouble whenever $\kappa \approx 1/\mathbf{u}$ (where \mathbf{u} is the computer's unit round off error, that is $1 + \mathbf{u} = 1$), while the method of normal equations is less robust running into trouble whenever $\kappa \approx 1/\sqrt{\mathbf{u}}$. The two methods produce comparable inaccuracies when applied to large residual, ill-conditioned problems. Golub and van Loan also demonstrate that the condition number grows if a column is added to the force matrix (that is, an extra load is added to the system).

If the system of equations is rank deficient (that is, at least one of the rows from the force matrix is a linear combination of the remaining rows), then the LS problem has an infinite number of solutions. Singular value decomposition (SVD) is particularly useful for rank deficient problems since it provides a neat expression for the LS solution and

the norm of the minimum residual [33, p. 242]. (Appendix D.1 contains details of the least squares SVD solution.)

From Equation (2.1) the stress at the zeroth gauge, in terms of loads, is given by $\sigma_0 = \{A_0\}^T \{f\} + \{B_0\}^T \{g\}$, where $\{A_0\}$ and $\{B_0\}$ are the load and acceleration coefficient vectors for the zeroth stress, and $\{f\}$ and $\{g\}$ are the force and acceleration vectors. (Note that the load vector has been partitioned into a force and acceleration vector, since we will in general know the acceleration vector. In contrast we will not know the force vector, at least not after the force coefficient matrix correlation is set up.) Similar expressions apply to the remaining stresses so that

$$\{\sigma\} = [A]\{f\} + [B]\{g\},$$

where curly and square brackets denote vector and matrices respectively, $\{\sigma\} = \{\sigma_1 \ \sigma_2 \ \sigma_3 \ \sigma_4 \ \sigma_5 \ \sigma_6\}^T$ is the stress vector, $[A] \in \mathbb{R}^{6 \times 6}$ and $[B] \in \mathbb{R}^{6 \times 2}$ are the force and acceleration coefficient matrices respectively, and $\{f\} = \{f_1 \ f_2 \ f_3 \ f_4 \ f_5\}^T$ and $\{g\} = \{g_1 \ g_2\}^T$ are the force and acceleration vectors respectively. Initially we will use only six of the seven stress equations so that the force coefficient matrix A is square. Also note that the stress vector σ has components σ_i , $\sigma_2, \dots, \sigma_6$, which denote *any* six stress equations, not necessarily the first six. Assuming the force coefficient matrix is invertible, solving for the force vector in terms of the stress vector gives

$$\{f\} = [A]^{-1}(\{\sigma\} - [B]\{g\}).$$

And hence the stress at the zeroth gauge in terms of the stress vector is

$$\sigma_0 = \{A_0\}^T [A]^{-1}(\{\sigma\} - [B]\{g\}) + \{B_0\}^T \{g\}.$$

The accelerations need not have been partitioned as they have been above; we could have left them in the loading matrix. However, because we can normally easily obtain the accelerations, we might as well subtract them from the system we are trying to solve (as was done in the above expression). The above formulation should result in a more stable system than would arise if the accelerations had been left in the loading matrix as unknowns.

To make the following procedures clearer let's ignore the acceleration. We may then rewrite the zeroth stress as

$$\sigma_0 = \{A_0\}^T [A]^{-1} \{\sigma\}. \quad (2.2)$$

2.5 Stress Estimation with Unknown External Load

If all we know are the stresses at a certain number of locations then it is possible to determine the stresses at still other locations. More specifically, if we know the stresses at K strain gauge locations then the stress at a different location, say the zeroth location, is given by

$$\begin{aligned}\sigma_0 &= \alpha_1\sigma_1 + \alpha_2\sigma_2 + \cdots + \alpha_K\sigma_K \\ &= \{\alpha\}^T \cdot \{\sigma\},\end{aligned}\tag{2.3}$$

where the α_k are constants, and $\{\alpha\}$ and $\{\sigma\}$ are the vectors containing the constant α_k and stresses σ_k respectively. Such a relation exists if there are as many strain gauges as there are input loads and the stresses on the left are of full rank. That is, no stress on the right hand side (RHS) is a linear combination of other stresses on the RHS, or in mathematical notation $\sigma_i \neq \sum_{k \neq i}^K \beta_k \sigma_k$ for any $i = 1, 2, \dots, K$, where the β_k are constants.

We now see why we termed the solution technique involving the load measurement the *matrix* technique, since Equation (2.2) involves a matrix. On the other hand, Equation (2.3), developed without external load knowledge, and only involving a vector, is termed the *vector* technique. The other difference to note is that we can think of the matrix technique as an *indirect* method, but the vector technique as a *direct* method. After all, the matrix and vector techniques yield the same results under ideal conditions (no noise), and so developing the force coefficient matrix seems an unnecessary step in the matrix technique for producing the same output as the vector technique.

3. Numerical Example of a 2-D Helicopter Truss

In this section we numerically simulate stresses (at strain gauge locations) on a 2-D helicopter truss (using the information derived in Appendix B) to determine the stability properties of developing a stress transfer function. All numerical values given in this section have been non-dimensionalised. The pin-joint locations of a simple truss (see Figure B.1) are shown in Table 3.1, while Table 3.2 shows the location of the two point masses and eight strain gauge locations.

	A	B	C	D	E	F	G	H
x	0	3	2	2	2	7.5	3.6	3.3
y	0	0	1	0	1.5	0.8	0.6	0.9

Table 3.1 Location of helicopter truss pin-joints.

	m_{AC}	m_{AE}	G_0	G_1	G_2	G_3	G_4	G_5	G_6	G_7
x	0.5000	0.5000	2.0000	1.0000	2.5000	2.6667	1.5000	2.4333	3.0750	3.4500
y	0.2500	0.0000	0.5000	0.5000	0.0000	0.3333	0.0000	0.9667	0.2250	0.4500

Table 3.2 Location of helicopter truss masses and strain gauges.

The two masses were $m_{AC}=9$ and $m_{AE}=7$, and all beam members were circular tubes (outer radius 0.015 and thickness 0.005) with a cross-sectional area of 392.7×10^{-6} and a second moment of area of 31.91×10^{-9} . Using these physical properties the stress at the eight strain gauge locations (shown below with five significant figures) are

$$\sigma_0 = -235.06 \times 10^3 P_m + 117.53 \times 10^3 P_x + 2.5465 \times 10^3 P_y, \quad (3.1)$$

$$\begin{aligned} \sigma_1 = & -1.8980 \times 10^3 P_m + 2.8471 \times 10^3 P_x - 529.74 \times 10^3 g_x + 1.0595 \times 10^6 g_y \\ & -1.8980 \times 10^3 T_m + 1.5184 \times 10^3 T_x - 8.5412 \times 10^3 T_y, \end{aligned} \quad (3.2)$$

$$\begin{aligned} \sigma_2 = & -848.83 P_m + 1.2732 \times 10^3 P_x + 156.71 \times 10^3 P_y + 1.9099 \times 10^3 g_x \\ & + 270.42 \times 10^3 g_y + 1.6977 \times 10^3 T_m + 1.1884 \times 10^3 T_x + 7.6394 \times 10^3 T_y, \end{aligned} \quad (3.3)$$

$$\begin{aligned} \sigma_3 = & 1.2004 \times 10^3 P_m - 1.8006 \times 10^3 P_x - 2.7009 \times 10^3 g_x + 5.4019 \times 10^3 g_y \\ & + 1.5005 \times 10^3 T_m - 1.2004 \times 10^3 T_x + 6.7524 \times 10^3 T_y, \end{aligned} \quad (3.4)$$

$$\sigma_4 = 1.6977 \times 10^3 P_m + 235.06 \times 10^3 P_y + 1.9099 \times 10^3 g_x + 818.89 \times 10^3 g_y + 1.6977 \times 10^3 T_m + 1.1884 \times 10^3 T_x + 7.6394 \times 10^3 T_y, \quad (3.5)$$

$$\sigma_5 = -2.7668 \times 10^3 T_m + 2.2135 \times 10^3 T_x - 12.541 \times 10^3 T_y, \quad (3.6)$$

$$\sigma_6 = -4.6974 \times 10^3 T_m - 268.42 T_x - 17.112 \times 10^3 T_y, \quad (3.7)$$

and

$$\sigma_7 = 6.0021 \times 10^3 T_m + 600.21 T_x + 25.209 \times 10^3 T_y. \quad (3.8)$$

Using either the external loads or the stresses (from gauges 1 to 7) to set up a coefficient matrix or vector respectively, we will develop a stress transfer function between the zeroth gauge and six other gauges.

3.1 Noiseless Stress Estimations

In this section we investigate what problems arise when we try to estimate stress, using measurements with no noise (either in the stress measurements or the load measurements). Then we investigate what effect measurement noise has on our stress estimation models.

Assuming no measurement noise we can readily derive the stress equations given by Equations (3.1)–(3.8). A small amount of work quickly shows that the stress equations σ_1 , σ_3 , and σ_5 are linearly dependent; in fact, the following relation holds

$$\sigma_1 = -1.5811\sigma_3 - 0.17150\sigma_5.$$

Thus if we eliminate any one of the stress equations 1, 3, or 5 the resulting force coefficient matrix will be invertible, because the system will then have full rank. What would happen if we eliminated any other row (that is *not* 1, 3, or 5), say for example the seventh stress equation σ_7 ? Then the resulting force coefficient matrix A would be a non-unique linear transformation, with the null space vector (explained below) given by

$$\{n\} = \{-0.12308 \quad 0.00400014 \quad -0.18462 \quad -0.24616 \quad -0.24616 \quad 0.91080\}^T.$$

By definition the matrix $[A]$ maps the null space vector $\{n\}$ onto the zero vector $\{0\}$, that is $[A]\{n\} = \{0\}$. Thus if $[A]\{x\} = \{b\}$, then for any scalar value α the vector $\{x\} + \alpha\{n\}$ has the same solution under the linear transformation A . In other words, if $\{y\} = \{x\} + \alpha\{n\}$

then the product $[A]\{y\}$ also equals $\{b\}$, despite the fact that $\{x\}$ and $\{y\}$ are different vectors.

If there are more stress equations than unknowns, then singular value decomposition (SVD), see Golub and van Loan [33, pp. 246–248], is one way to determine which rows to eliminate. The number of singular values above some small lower limit (see Appendix D.1 for further details on SVD) gives the rank of the matrix. As Golub and van Loan state: 'Near rank deficiency in A cannot escape detection when the SVD of A is computed'. The 2-norm *condition number* κ of the matrix A , given by the ratio of largest to smallest singular values (see Appendix D.1), is a convenient by-product of using SVD to determine the rank of A .

To improve stability properties, we choose the resulting coefficient matrix that yields the smallest condition number. Sequentially eliminating either the first, third, or fifth stress equations (σ_1 , σ_3 , and σ_5) from the force coefficient matrix yields condition numbers $\kappa=569.97$, $\kappa=562.97$, and $\kappa=1805.8$ respectively. So to minimise the condition number we eliminate the third stress equation σ_3 , which results in the force coefficient matrix

$$A = \begin{bmatrix} 2847.1 & 0 & -1898.0 & 1518.4 & -8541.2 & -1898.0 \\ 1273.2 & 156700. & -848.83 & 1188.4 & 7639.4 & 1697.7 \\ 0 & 235060. & 1697.7 & 1188.4 & 7639.4 & 1697.7 \\ 0 & 0 & 0 & 2213.47 & -12450.8 & -2766.84 \\ 0 & 0 & 0 & -268.42 & -17112. & -4697.4 \\ 0 & 0 & 0 & 600.21 & 25209. & 6002.1 \end{bmatrix}.$$

The columns represent the input loads P_x , P_y , P_m , T_x , T_y , and T_m from left to right respectively. The above matrix has linearly independent rows and a 2-norm condition number $\kappa=562.97$.

From the zeroth stress equation σ_0 , given by Equation (3.1), we know that the force coefficient vector is given by $A_0^T = 10^3 \{117.53 \ 2.5465 \ -235.06 \ 0 \ 0 \ 0\}$, and using Equation (2.2) we have that

$$\sigma_0 = 10^{-3} \begin{bmatrix} 117.53 \\ 2.5465 \\ -235.06 \\ 0.0000 \\ 0.0000 \\ 0.0000 \end{bmatrix}^T \begin{bmatrix} 614.67 & -589.05 & 392.70 & -346.36 & 62.091 & 138.84 \\ -2.8538 & 6.3814 & 0.0000 & -0.48943 & -2.0180 & -4.5123 \\ 395.15 & -883.57 & 589.05 & -158.12 & 93.137 & 208.26 \\ 0.0000 & 0.0000 & 0.0000 & 391.54 & 124.18 & 277.68 \\ 0.0000 & 0.0000 & 0.0000 & -30.119 & 372.55 & 277.68 \\ 0.0000 & 0.0000 & 0.0000 & 87.344 & -1577.1 & -1027.4 \end{bmatrix} \begin{bmatrix} \sigma_1 \\ \sigma_2 \\ \sigma_4 \\ \sigma_5 \\ \sigma_6 \\ \sigma_7 \end{bmatrix}$$

$$\sigma_0 = -20.6479\sigma_1 + 138.478\sigma_2 - 92.3077\sigma_4 - 3.54108\sigma_5 - 14.6003\sigma_6 - 32.6472\sigma_7 \quad (3.9)$$

As can be seen from the above expression the third stress equation σ_3 was not used to solve the above system, thus yielding a system with full rank and the smallest possible condition number. Remember that the above solution was produced with no noise in the system. We now investigate the effects of noise in the both load and stress measurements.

3.2 Noisy Stress Estimations with Known External Load (matrix technique)

In this report we refer to randomly generated numbers. All random numbers were generated with a pseudo-random number generator defined within the *Mathematica* package [34]. For consistency, all comparisons involving random numbers were carried out with the same set (or same initial set if subsequent comparisons involved larger sets) of random points. The same set of random points was easily re-generated by seeding the pseudo-random number generator with the same starting integer.

Furthermore, assume we have *a priori* knowledge of the exact force coefficient matrix, and hence know that eliminating the third stress equation σ_3 leads to the smallest condition number. In reality no such *a priori* knowledge would be available, and thus an appropriate way to determine which combination of strain gauges minimises the condition number for noisy data needs further investigation. However, we later show that for *this* particular truss, eliminating the third stress equation does indeed lead to 'optimum' results.

Input loads were randomly generated uniformly in the range $[-10, +10]$ for each of the six input loads $P_x, P_y, P_m, T_x, T_y,$ and T_m , resulting in 1000 different load sets. Each set contained six input loads, for simplicity the accelerations g_x and g_y were set to zero. These random input loads (together with statics) were then used to generate 1000 stress sets (each set containing seven stresses from gauges 0 to 7 excluding gauge 3). In summary, we randomly selected the input loads, but the resulting truss stresses were determined using statics. We interchangeably refer to a load set or a stress set as a load point or stress point respectively. White noise was then added to both the resulting loads and stresses, at 5% and 10% of the recorded value. The stress equations were again derived, this time using a least squares (LS) fit of these noisy data sets. (The in-built *Mathematica* function `Fit[]`, based on the pseudo-inverse of the input data, performs the LS fit.) The force coefficient matrices for 5% and 10% noise are given respectively by

$$A_{5\%} = \begin{bmatrix} 2847.9 & -20.972 & -1883.3 & 1515.5 & -8538.4 & -1919.4 \\ 1209.9 & 156880. & -947.81 & 967.17 & 7928.3 & 1894.3 \\ -93.037 & 235310. & 1564.1 & 850.91 & 8066.6 & 1980.9 \\ 5.3447 & -31.073 & 27.757 & 2204.8 & -12450. & -2806.8 \\ -1.1641 & -38.491 & 32.788 & -286.31 & -17117. & -4745.3 \\ 0.10014 & 55.116 & -48.468 & 629.78 & 25216. & 6068.7 \end{bmatrix}$$

and

$$A_{10\%} = \begin{bmatrix} 2844.1 & -41.703 & -1866.1 & 1510.0 & -8521.2 & -1937.1 \\ 1160.9 & 156790. & -1047.0 & 758.66 & 8206.4 & 2097.7 \\ -160.52 & 235170. & 1424.4 & 533.97 & 8484.7 & 2276.4 \\ 11.159 & -62.219 & 53.925 & 2193.0 & -12427. & -2841.1 \\ -1.2640 & -77.541 & 63.402 & -302.47 & -17093. & -4783.8 \\ -1.4135 & 111.01 & -93.805 & 656.54 & 25179. & 6123.0 \end{bmatrix}.$$

We want to determine how 'close' the above approximations are to the exact solution. Thus define the normalised error for the above approximations as

$$\varepsilon = \frac{\|Ef\|_2}{\|Af\|_2}, \quad (3.10)$$

where A is the exact force coefficient matrix, f is a load vector, and E is the error matrix defined as $E = \hat{A} - A$ where \hat{A} is some approximation to A (in our case either $A_{5\%}$ or $A_{10\%}$). Finally note that we have used the 2-norm in the above definition, where the 2-norm of a vector x is defined as $\|x\|_2 = \sqrt{x \cdot x}$. The above normalised error measures the accuracy of our approximate force coefficient matrix \hat{A} compared to A (the exact force coefficient matrix). We can now investigate the effects of white noise on error. Figure 3.1 shows the normalised error for approximations with both 5% and 10% white noise for 10,000 randomly generated unit load vectors (these random vectors were generated as discussed earlier). As an aside, plots of the normalised error distribution (akin to Figure 3.1) using 100, 300, and 1000 random unit load vectors (instead of 10,000) show excellent agreement with the distribution resulting from the 10,000 random unit load vectors. That is, the distribution appears to be independent of the number of points used to generate it.

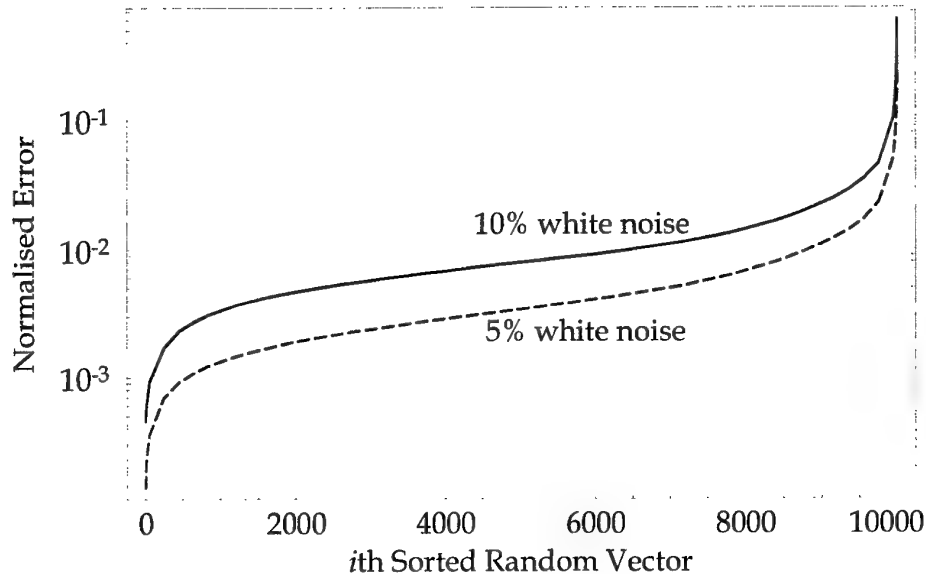


Figure 3.1 Sorted normalised error versus i th random vector for 10,000 random vectors. The data used in the approximation includes either 5% or 10% white noise.

As we would expect, Figure 3.1 shows the approximation with more noise produces larger errors. Figure 3.1 also shows that the regions of large error are highly localised since only a small portion of the data registers large errors. For example, for data with 10% white noise, less than 1% of the data have error exceeding 10%. Consideration of the singular values shows that most ill-conditioned exact matrices A would yield localised error regions. A geometric assessment of the singular values also leads to the conclusion that the two maximum error regions become more localised as the dimensions of the coefficient matrix increase, especially for ill-conditioned systems. (For further details see Appendices E.1.) Finally, to emphasise the point, note that more than 95% of the 10%-white-noise data (98% of the 5%-white-noise data) has less than 5% error.

Appendix E shows that the normalised error, as defined in Equation (3.10), for any matrix approximation \hat{A} has two maxima of equal magnitude but their respective vectors point in exactly opposite directions. Using this result we can safely use any maximisation technique to produce the global maximum. Table 3.3 shows this maximum normalised error (and associated vector) for data with 5% white noise. The effect of the number of data points in developing the approximate force coefficient matrix was investigated. The first column shows the number of points used to develop the approximation (or in other words the approximation order). The second column shows the maximum possible error for any unit force vector. The last column shows the direction of the unit force vector corresponding to the maximum error. As expected, increasing the number of points used in the approximation reduced the error, in essence averaging out the white noise. Also, contrary to expectations, the vectors

associated with the maximum error do not appear to converge with an increasing number of points in the approximation. This small sample may suggest that the error matrix E is uniformly distributed as the approximation order increases, which is an assumption we made in Appendix E.1 to arrive at the result suggesting that the maximum error region was localised.

Apx. Pts.	Max. Error	Direction of Max. Error
100	3.386	$[-0.1452, -9.357 \times 10^{-4}, -0.1602, 0.1685, 0.2301, -0.9337]^T$
300	1.213	$[-0.6286, -4.018 \times 10^{-3}, -0.6897, -0.04531, 0.08791, -0.3454]^T$
1000	0.6686	$[0.2604, -3.522 \times 10^{-3}, 0.3524, 0.1478, 0.2134, -0.8605]^T$
3000	0.2984	$[0.1976, 8.507 \times 10^{-4}, 0.1858, -0.1961, -0.2249, 0.9151]^T$

Table 3.3 Maximum normalised error and associated vector for several different approximations using a different number of points.

A graphical representation of the Table 3.1 results is shown in Figure 3.2. This figure shows the variation of normalised error (dotted black line) versus the number of points used in the approximation of the force coefficient matrix for data with 5% noise.

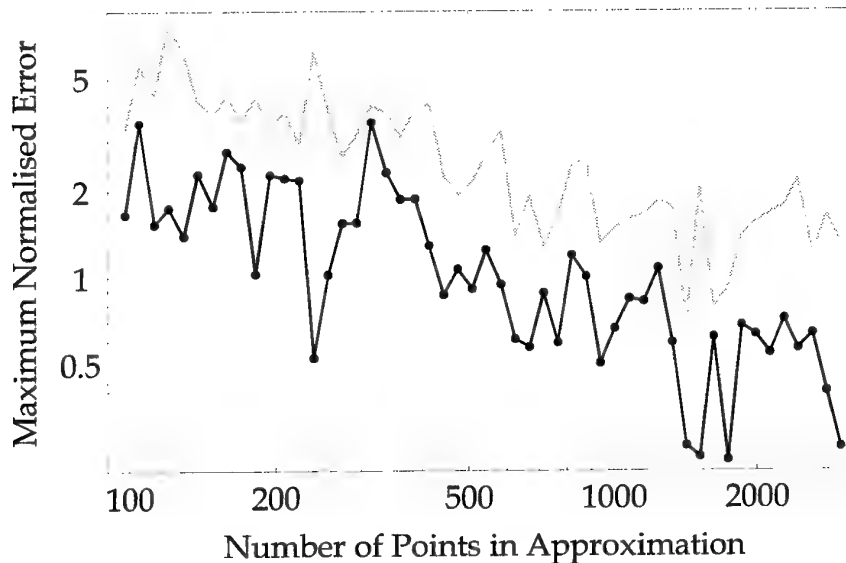


Figure 3.2 Plot of maximum normalised error (dotted black line) for several approximations of the force coefficient matrix using different number of points in the approximation. The light grey line shows an approximation to the normalised error upper bound (simply given by the ratio of singular values).

Again we see that the maximum normalised error decreases as the number of points in the approximation increases. We see, however, that although the error decreases on average, from point to point the error fluctuates seemingly randomly. For example,

using a 240 point approximation the maximum normalised error was found to be 0.5238, as compared to an error of 0.6338 for a 2617 point approximation. The light grey line above the maximum normalised error line (dotted black line) is a bound obtained by dividing the largest singular value of the error matrix by the smallest singular value of the true force coefficient matrix. As can be seen this maximum bound provides a crude approximation to the maximum error.

Figure 3.3 shows how the error is distributed for different approximation orders using data with 5% white noise. The 10,000 random points were sorted by the magnitude of the normalised error so as to obtain the distribution plots. Again, the error decreases as more points are used in the development of the coefficient matrix approximation. All approximations show good agreement with the exact solution, with even the 100 point approximation registering less than 10% error for more than 98% of the data.

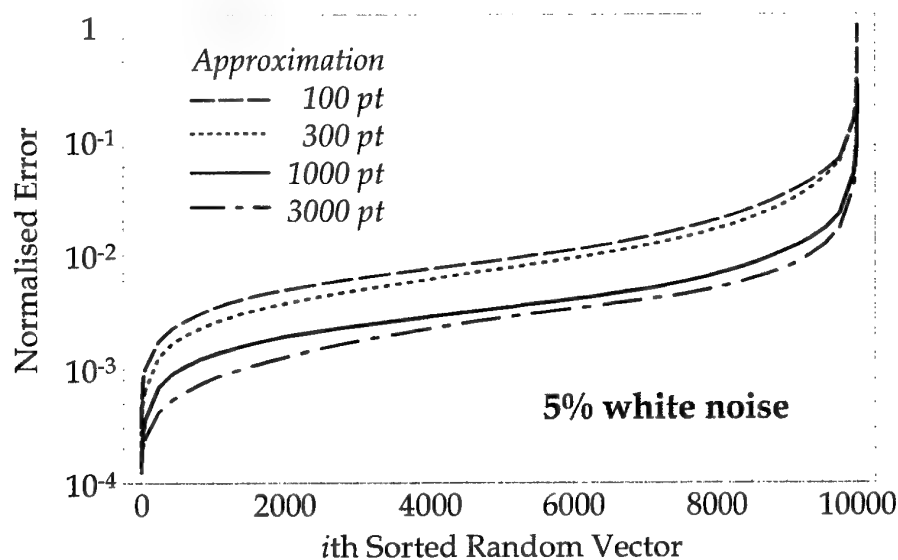


Figure 3.3 Normalised error for 10,000 random unit force vectors using 100, 300, 1000, and 3000 point approximations of the force coefficient matrix. The data set used to develop the approximate force coefficient matrix contained 5% white noise.

Although we have excellent approximations of the coefficient matrix, remember from Equation (2.2) that we need to invert the coefficient matrix. Performing a similar analysis on the inverted coefficient matrix produces less favourable results. Figure 3.4 shows the normalised error distribution (normalised against the exact inverse of the coefficient matrix) for the inverted approximate coefficient matrices. As can be seen only the 3000 point approximation gives results with tolerable errors. This result might be expected from consideration of the unstable procedure of matrix inversion.

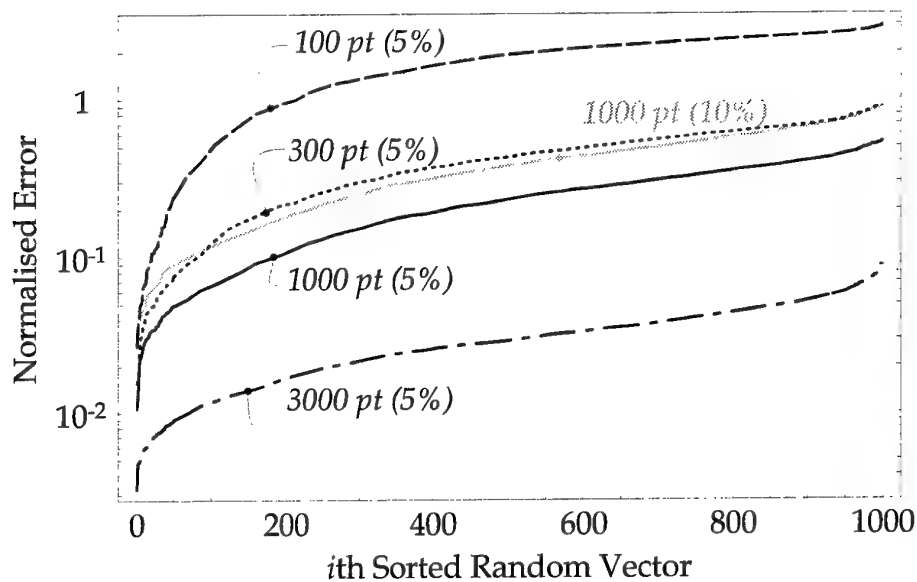


Figure 3.4 Normalised error for 1000 random unit force vectors using the inverse of the approximate force coefficient matrices. The approximations use 100, 300, 1000, and 3000 points for data with 5% white noise, and 1000 points for data with 10% white noise.

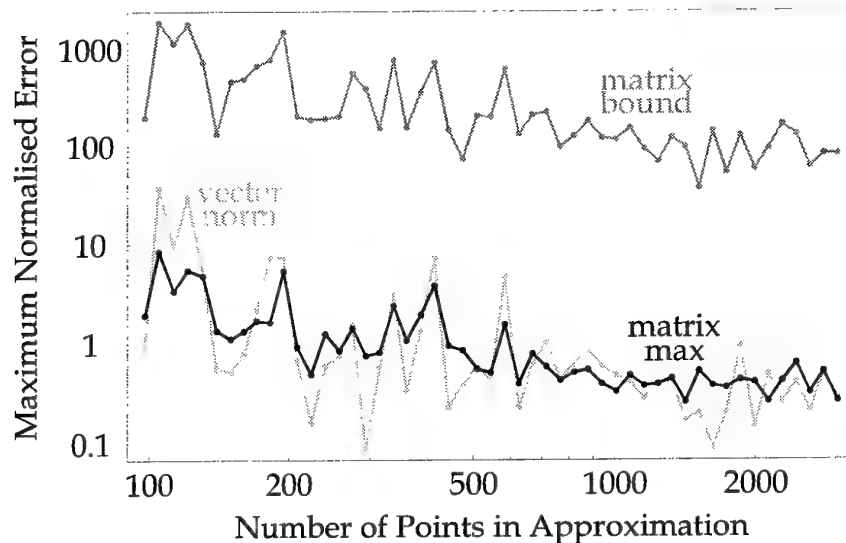


Figure 3.5 Plot of maximum normalised error (black line) for several approximations of the force coefficient matrix using different number of points in the approximation. The dark grey line shows an approximation to the normalised error upper bound (simply given by the ratio of singular values). The light grey line shows the vector norm for the same approximations.

Similar to Figure 3.2 we can generate a plot of maximum normalised error versus the number of points in the approximation for the inverse approximate coefficient matrix; the result is shown in Figure 3.5. As before there are only two maxima (both the same magnitude) on the normalised error surface generated by unit load vectors. The matrix maximum was thus simply found by maximising this error surface. The normalised error matrix bound is again the ratio of the largest singular value of the error matrix to the smallest singular value of the exact matrix.

A vector norm would not only include the inverse of the approximate force coefficient matrix, but would also incorporate the least squares approximate of the stress at the zeroth strain gauge. We begin by defining an appropriate measure of the approximation's error. From Equation (2.3) the stress at the zeroth gauge was given by $\sigma_0 = \alpha_1 \sigma_1 + \alpha_2 \sigma_2 + \dots + \alpha_K \sigma_K$, which may be written in vector notation as $\sigma_0 = \alpha^T \cdot \sigma$, where $\alpha = [\alpha_1 \ \alpha_2 \ \dots \ \alpha_K]^T$ is the vector of coefficients and $\sigma = [\sigma_1 \ \sigma_2 \ \dots \ \sigma_K]^T$ is the vector of stresses, for the gauges 1, 2, ..., K respectively. Given an approximation $\hat{\sigma}_0$ to the exact stress σ_0 we want to determine some sort of normalised accuracy of that approximation. We cannot simply use the normalised error definition $\epsilon_{\max} = \max_{\|\sigma\|=1} (\hat{\sigma}_0 - \sigma_0) / \sigma_0$ since the denominator becomes zero for some unit stress vectors (given by $\|\sigma\|=1$). However, expanding this error definition $(\hat{\sigma}_0 - \sigma_0) / \sigma_0 = (\hat{\alpha}^T \cdot \sigma - \alpha^T \cdot \sigma) / (\alpha^T \cdot \sigma) = [(\hat{\alpha} - \alpha)^T \cdot \sigma] / (\alpha^T \cdot \sigma)$, where $\hat{\alpha}$ is the $\hat{\sigma}_0$ approximation's vector of coefficients, we obtain the genesis for an appropriate *normalised error* definition

$$\epsilon_{\max} = \sqrt{\frac{(\hat{\alpha} - \alpha)^T \cdot (\hat{\alpha} - \alpha)}{\alpha \cdot \alpha}}. \quad (3.11)$$

The above definition may be thought of a vector norm. Note that this definition considers only the coefficients, and is thus extremely simple to calculate.

Values of the normalised error (vector norm) versus the approximation order are plotted as the light grey line in Figure 3.5. Note the close relation between the maximum error of the normalised matrix (black line) and the vector norm. This suggests that most of the error comes from the matrix inversion procedure as suspected.

Finally, to visually gauge the accuracy of some of the approximations a scatter plot (of exact stress versus approximate stress) for two approximations (1000 and 3000 point approximations) is shown in Figure 3.6. This figure emphasises the result shown in Figure 3.4, which depicts large errors for the 1000 point approximation.

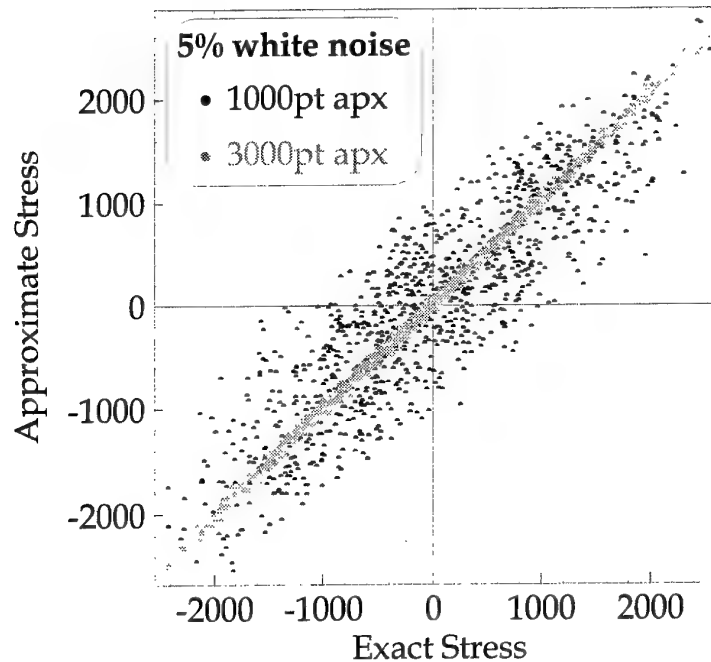


Figure 3.6 Scatter plot of 1000 random unit force vectors; the horizontal axis shows the exact stress value while the vertical axis shows the approximated stress value. Approximations of the force coefficient matrix using 1000 (black) and 3000 (grey) points are compared for data with 5% white noise.

3.3 Noisy Stress Estimations with Unknown External Loads (vector technique)

We produce some unexpected results in this section, namely that the more arduous method of the previous section provides better results than stress estimation without the force coefficient matrix.

Figure 3.7 uses the normalised error definition given by Equation (3.11) to demonstrate the relation between percentage noise in the data and normalised error. There are two disturbing results in this plot. Firstly, the normalised error tapers to approximately unity as the noise increases above approximately 1%. The second disturbing result is that the accuracy of the approximation appears to be independent of the number of points used to develop that approximation, that is, accuracy is independent of approximation order!

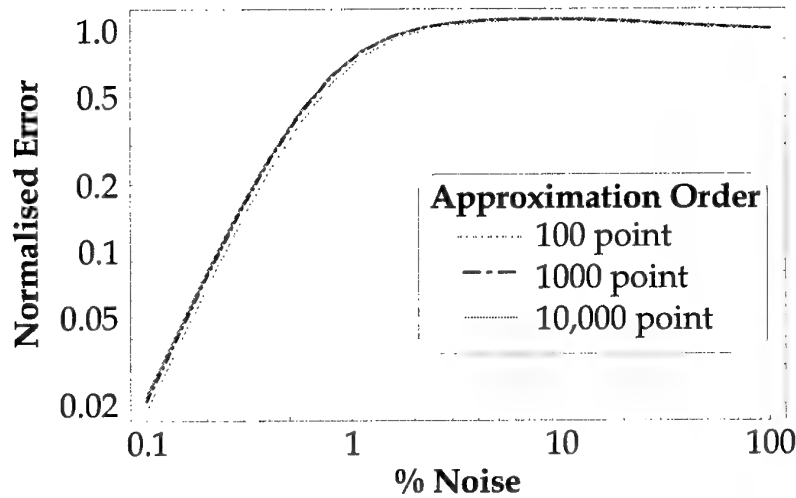


Figure 3.7 Variation of normalised error with percentage noise for 100, 1000, and 10,000 point stress approximations.

The first of these disturbing results may actually be explained on closer consideration of what is happening as the signal-to-noise ratio of the data set decreases. As we increase the noise the stresses from the six gauges (used to approximate the stress for the zeroth gauge) become uncorrelated with the stress at the zeroth gauge. Let's consider a simple example of what happens to the linear least squares fit of uncorrelated data.

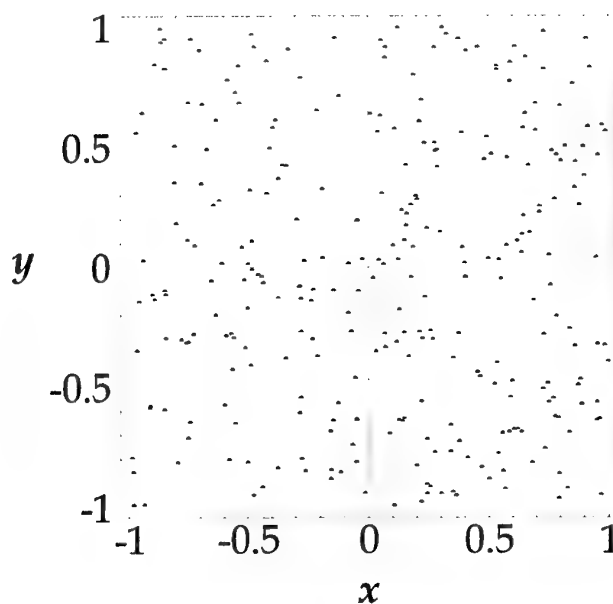


Figure 3.8 Example of uncorrelated data, for which the least squares linear fit is $y=A+Bx$. As the number of approximation points tends to infinity the coefficients A and B tend to zero.

Figure 3.8 shows 300 points whose x and y coordinates vary randomly (and independently) between -1 and 1 . The best linear fit, based on least squares, is given by $y = -0.0277 - 0.0254x$. As can be seen (and is intuitively obvious), the line with near zero slope best fits these data. If the amount of data increases and the x and y coordinates becomes more uncorrelated, then in the limit the slope approaches zero. Referring back to Equation (3.11) we see that if the approximation's coefficient vector $\hat{\alpha}$ tends to zero then the normalised error will tend to unity. This fact then explains why in Figure 3.7 the error tends to unity.

At first it was thought that the original linear dependence of the gauge stresses was to blame for these poor results as soon as any noise entered the system. Figure 3.9 plots the normalised errors upon deletion of different gauges compared (as a ratio) to the normalised errors from deleting the 3rd gauge. Figure 3.9 verifies the fact that the smallest normalised errors are obtained by eliminating the 3rd gauge, as we had predicted using the condition number analysis in § 3.1.

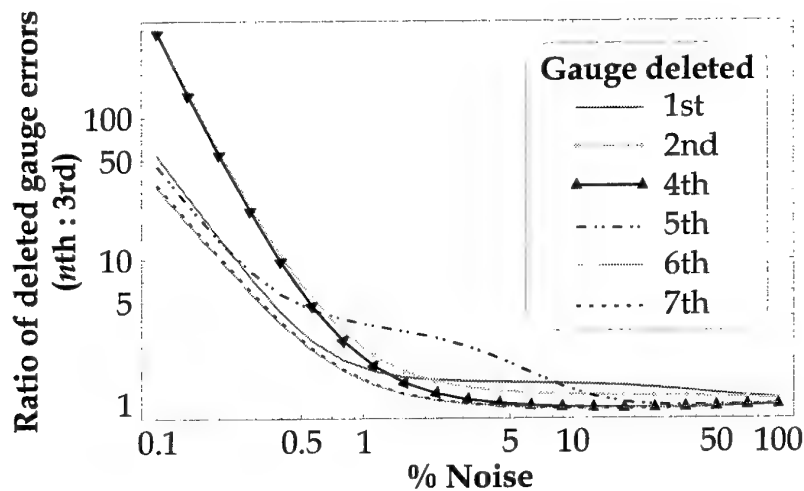


Figure 3.9 Comparison of errors when different gauges are deleted. The comparison shows the ratio of the error from deleting the n th gauge to the error from deleting the 3rd gauge.

Figure 3.10 compares the exact solution (the horizontal axis) to the estimated solution (the vertical axis) using 1000 randomly selected stresses (for gauges 1–7 excluding 3) ranging between -10 and 10 . The plots on the left and right show the results when the data sets used to develop the approximation contained 5% and 0.5% white noise respectively. For each plot two approximations were developed, one using 1000 points (shown as black dots) and the other using 3000 points (shown as grey dots). Figure 3.10 emphasises the fact that even a small amount of noise is all that's needed to completely corrupt the approximation. These plots also show that the stress is consistently underestimated when the approximations were developed with data containing both

5% and 0.5% noise. For example, for the 0.5% noise plot when the structure is experiencing 2000 units of stress, the stress estimated is less than 1200 units of stress (on average). The under-estimation is even worse for the 5% noise plot. Perhaps this under-estimation is related to the near zero coefficient vector of the approximation?

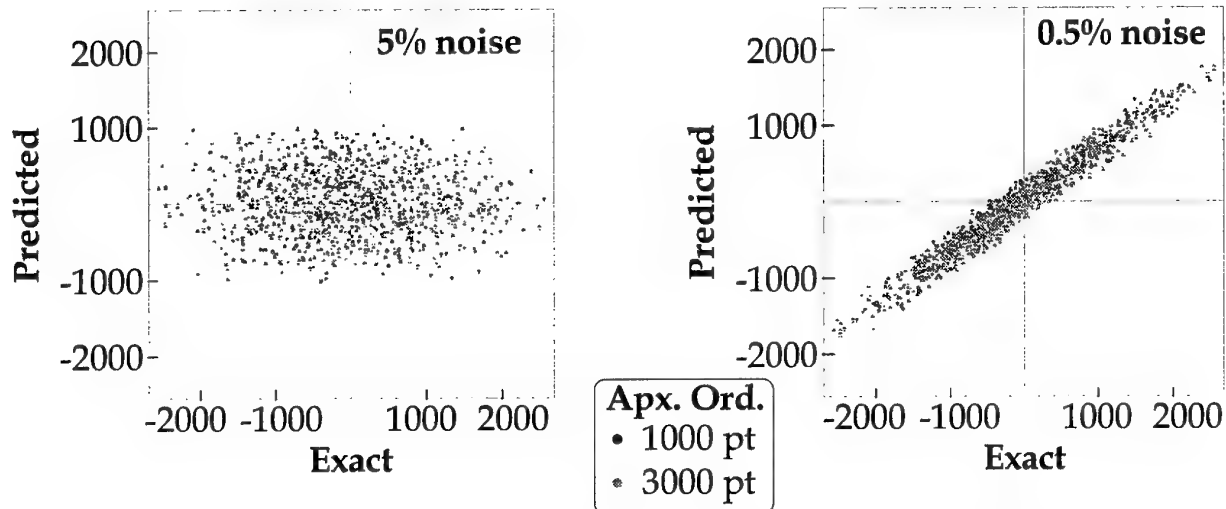


Figure 3.10 Comparison of exact solution and estimated solution for 1000 random data points with 5% noise (left) and 0.5% noise (right), using 1000 points (black) and 3000 points (grey) approximations.

In order to gain some understanding of these anomalous results we investigate a simpler model (yielding a 2x2 matrix system) in the next section.

4. Preliminary Results of a Simplified Truss

In this section we develop a five-member simple truss to further investigate the properties of the vector and matrix solution techniques.

Figure 4.1 illustrates the statically determinate five-member truss we will use in this section. All joints are pinned, joint *D* is grounded via a pin restraint, and joint *B* is grounded via a roller bearing. The horizontal distance from joint *D* to joints *A*, *B*, and *C* are 1, 2, and 1.1 respectively. All distances have been non-dimensionalised by the vertical distance from joint *D* to joint *C*, and thus this vertical distance is unity. We apply a horizontal force of magnitude P_x at joint *C*, and a vertical force of magnitude P_y at joint *A*. We will determine the force in member *CD* using the forces in members *AD* and *AB*. (The choice of truss and forces will be explained in a future report. This section merely reports preliminary results of a numerical simulation.)

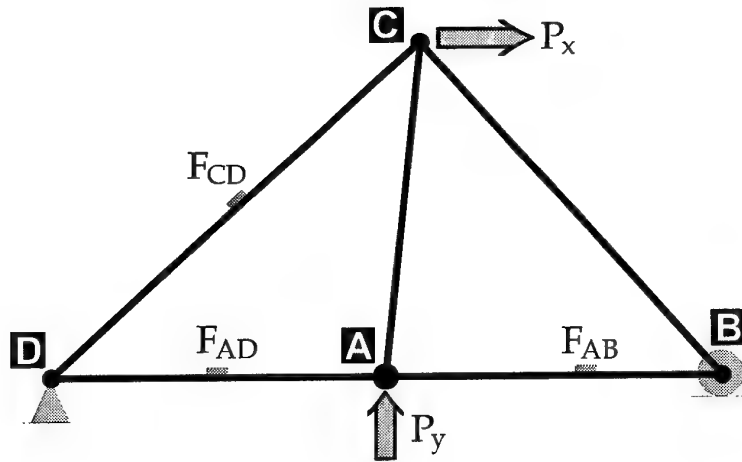


Figure 4.1 Simplified truss: The horizontal distances from joint *D* to joints *A*, *B*, and *C* are 1, 2, and 1.1 respectively. The vertical distance from joint *D* to joint *C* is 1.

The exact forces within the members *AD*, *AB*, and *CD* are given respectively by

$$F_{AD} = 0.4500P_x - 0.5500P_y, \quad (4.1)$$

$$F_{AB} = 0.4500P_x - 0.4500P_y, \quad (4.2)$$

and

$$F_{CD} = 0.7433P_x + 0.7433P_y. \quad (4.3)$$

Hence we can solve for the force in member CD in terms of the forces in members AD and AB yielding the relation $F_{CD} = -14.87F_{AD} + 16.52F_{AB}$. (Note that these results are quoted to four significant figures.) The above relation is recovered whenever least squares (LS) is used to fit input and output data with no noise. (The input data are given by the forces F_{AB} and F_{AD} , while the output data are determined from the resulting force F_{CD} .) Using noisy data, however, we find that as we increase the number of points in the LS fit the vector method produces large errors. On the contrary, the matrix method results improve whenever the number of points used in the LS fit is increased.

Figure 4.2 shows the distribution (or frequency plots) of 1000 LS solutions for both the vector and matrix solution techniques. As before the input data (loads P_x and P_y) were randomly generated using a uniform distribution. The resulting loads in members AD , AB , and CD were determined using Equations (4.1)–(4.3). So that each input load pair (P_x, P_y) resulted in a *data point* of the form (F_{AD}, F_{AB}, F_{CD}) . Each LS solution used 128 data points to determine the fit. Both distribution plots divided the LS solution data into 16 data bins, and on a logarithmic scale, all bins were of the same width. In a statistical sense, the matrix technique produced smaller errors than the vector technique for the 128 point fit. Both the vector and matrix distributions are almost normal on a logarithmic scale. The slight skewness towards zero normalised error can be explained by the fact that the error is bounded from above, but it is still possible to obtain a solution with zero normalised error.

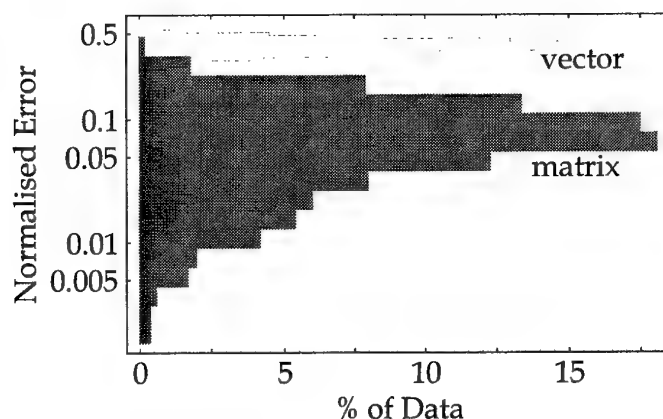


Figure 4.2 Distribution of 1000 least squares (LS) solutions. Each LS solution used 128 data points to determine the fit.

From this distribution we can easily determine the lowest outlier, first quartile (Q_1), the median, the third quartile (Q_3), and the upper most outlier. This distribution information allows us to estimate both spread and skewness. Repeating the above distribution analysis for fits using 2, 4, 8, ..., 1024 point approximations we can produce

the plot shown in Figure 4.3, which shows the distribution of normalised error for several approximation orders. Note that each approximation order plotted in Figure 4.3 consists of 1000 normalised errors for the LS fit.

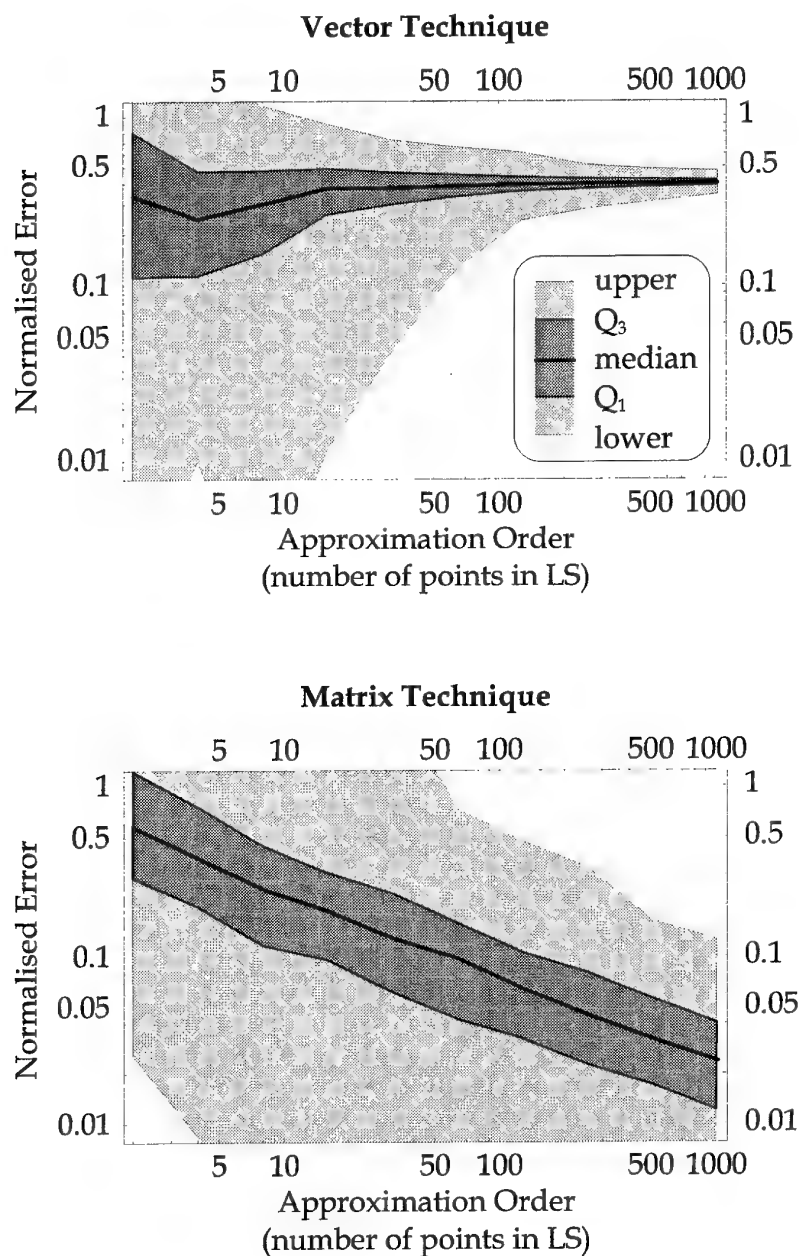


Figure 4.3 Comparison of the normalised error for the vector and matrix techniques. Shown are the distribution's upper and lower outliers (outer edges of light grey region), first and third quartile (outer edges of dark grey region), and median (thick line).

Although the spread of the error for the vector technique decreases as the number of data points increases, the error converges around a wrong solution. Thus, in a statistical sense (using the median), the error actually (slowly) increases as the number of points used in the LS fit increases. We see the reverse for the matrix technique, where, as expected, both the error and spread decrease with increasing information (again in a statistical sense).

Preliminary results suggest that this phenomenon occurs only when there is some collinearity within the input data, and is (surprisingly) independent of the condition number of the system. Initial results also suggest this drawback in using the vector technique can be overcome. The modified vector technique involves using the lowest number of data points possible in the LS fit (for our two-by-two system this means two data points). We obtain a set of these simple LS fits, then determine the median of this set. Figure 4.4 plots the normalised error of the modified vector technique for several approximation orders. As can be seen, the lowest order approximation is better than the high order approximations by almost an order of magnitude.

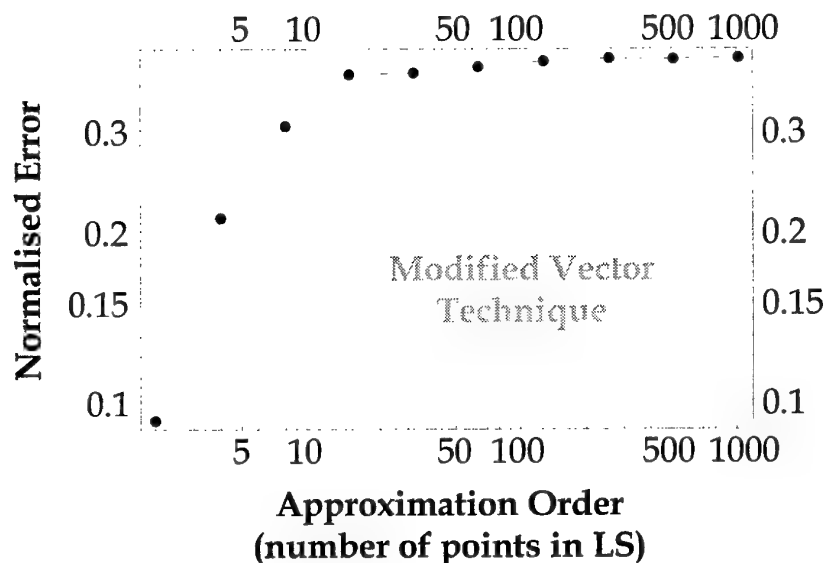


Figure 4.4 Plot of the normalised error (for the modified vector technique) versus least squares approximation order. Each particular approximation order point in this plot represents the normalised error of the median of 1000 least squares solutions.

Do not confuse these two last figures. In Figure 4.3 we have plotted the median (along with outliers and quartiles) of the distribution of normalised errors. In contrast, Figure 4.4 shows the normalised error of the median of the distribution of LS solutions versus approximation order. This modified approach also works for the matrix method and produces better results than the original matrix procedure. The advantages of this

modified procedure are that it is faster to implement, requires less information, and produces better results. A proof of this procedure will be given in a future report.

5. Discussion

In this brief section we summarise and expand on some of the topics already discussed.

The non-linear analysis suggested that we place all strain gauges away from buckling structures. We did not develop general guidelines on what a 'safe' distance from the buckling member would be, since we suspect that any such analysis would be both complex to undertake and largely problem-dependent. As such the choice of strain gauge locations requires engineering intuition and logic, and where feasible a finite element analysis check should be made.

We also showed that non-uniqueness effects need to be foremost in the investigator's mind when deciding which locations are amenable to solution by the stress transfer function method. Essentially, any structure for which we have more unknown loads than load equations would give rise to a non-uniqueness problem.

Linear independence of strain gauge measurements is critical if a stress transfer function is to be developed. However, we also noted that linear independence was insufficient when noisy measurements were involved. We need to further investigate the extent of system ill-conditioning that can be tolerated while still obtaining satisfactory solutions. That is, if we slightly perturb the exact force coefficient matrix (by adding noise), is it likely that the perturbed matrix will be close to an ill-conditioned matrix? An alternative direction of research might be: what structural characteristics cause the system of equations to become ill-conditioned in the first place? We have already mentioned inappropriate location of strain gauges as one possible suspect. Are there others, for example truss geometry, and if so can ill-conditioning effects be quantified or at least ordered (so as to prioritise effects)?

An initial investigation of ill-conditioning within the underlying system of equations (that is, the exact matrix A) showed that the matrix technique was more stable than the vector technique. For well-conditioned systems both methods yielded comparable results. Preliminary results have also shown that a modified vector technique can produce results that are better than the matrix technique. These initial results, however, require a more rigorous generalisation and associated validation, but go some way to explaining the results observed for the vector technique.

One reason for pursuing the vector technique over the matrix technique is the simplified coefficient vector construction (no knowledge of the external loading is required). Both experimentally and in the final implementation, the accurate application and measurement of external loads and measurement of stresses (the matrix technique) would require significant additional work when compared to taking only stress measurements (the vector technique). However, the highlighted ill-

conditioning problems would need to be addressed before the vector technique could be successfully implemented.

We know, at least for the near ill-conditioned system developed, that the errors from the vector technique did not improve when the approximation order was increased. It might prove profitable to pursue ideas based on the bootstrap method. (For a concise overview of the bootstrap method see Press *et al.* [35].) For example, would combining several low order approximations improve results, or could the data be reorganised to produce the true underlying distribution?

We know that the matrix and vector techniques are based on the same fundamental solution procedure (least squares), and that the final forms of these solutions are the same (a list of strain gauge coefficients). Why then is the matrix technique more stable than the vector technique (at least for the ill-conditioned problem in this report)? The only hypothesis that readily comes to mind is that the greater amount of information stored in the development of the force coefficient matrix helps to stabilise the subsequent inversion procedure. However, it is still hard to imagine that under some situations the indirect matrix technique should yield results that are superior to the direct vector technique.

We conclude this discussion section with several open-ended questions arising from the results of the preceding sections and the discussion within this section.

- How does noise affect the system's condition number?
- How do structural characteristics affect the ill-conditioning?
- Why is the error independent of the approximation order for the vector technique?
- Why did the vector technique under-estimate the results?
- Why does the matrix technique appear to be more stable than the vector technique?
- Are there situations under which the vector technique gives results superior to the matrix technique?
- Will a data analysis method based on the bootstrap method improve results?

6. Conclusion

Consideration of non-linear effects showed that buckling (whether local, as in beam flanges, or ordinary, as in the skin) would lead to a bi-linear stress response at best. As such we recommended all strain gauges set up to determine the stress response of any underlying linear (or almost-linear) system should be located away from the load paths of buckling structures. We were also able to demonstrate that indeterminate systems still remained linear, at worst complicating linear relationships and adding constants to the solution procedure. We also showed that under some conditions a static stress model would yield non-unique solutions if measurements were made outside the relevant structure. For a simply supported beam, we also determined when the static stress distribution model would provide a poor approximation of the dynamic stress distribution.

We examined two solution techniques, the matrix and vector techniques. We developed the stress transfer function (STF) for the matrix and vector techniques respectively, with and without external load information. Although the matrix technique was susceptible to noise, the error in the STF approximation could be reduced by increasing the approximation order (that is, the number of load-stress points in the least squares fit). In contrast, increasing the approximation order for the vector technique had an insignificant effect. For noisy data, the vector technique's STF improved only when the signal-to-noise ratio was well above realistic levels. Initial results seem to suggest that the poor performance of the vector technique was related to the ill-conditioned system of equations governing stress in the truss. The matrix method, however, seemed far less susceptible to this ill-conditioning. Finally, preliminary results also suggest that taking the median of a large number of low order approximations yields good results for both the matrix and vector techniques.

7. References

1. A. B. Cook, C. R. Fuller, W. F. O'Brien, and R. H. Cabell, 'Artificial Neural Networks for Predicting Nonlinear Dynamic Helicopter Loads', *AIAA Journal*, v.32, n.5, pp. 1072-77, May 1994.
2. C. T. Gunsallus and E. Robeson, 'AH-64A Rotating Load Usage Monitoring from Fixed System Information', *American Helicopter Society Structures Specialist Meeting*, Williamsburg, (A-93-27953), 28-30 Oct. 1991.
3. 'Black Hawk Structural Usage Monitor', *Sikorsky Aircraft Document*, SER-701760, 15 Sep. 1991.
4. H. Azzam, 'A Practical Approach for the Indirect Prediction of Structural Fatigue from Measured Flight Parameters', *Proceedings of the Institution of Mechanical Engineers, Journal of Aerospace Engineering*, v.211 (Part G), pp. 29-38, 1997.
5. R. H. Cabell, C. R. Fuller, and W. F. O'Brien, 'Neural Network Modelling of Oscillatory Loads and Fatigue Damage Estimation of Helicopter Components', *Journal of Sound and Vibration*, v.209, n.2, pp. 329-42, 1998.
6. L. A. Flitter, K. McCool, and D. J. Haas, 'Rotor Load System Monitoring Using a Neural Network Based Approach', *AIAA Modeling and Simulation Technologies Conference*, New Orleans, LA, AIAA Paper 97-3510, 11-13 Aug., 1997.
7. C. T. Gunsallus, W. L. Pellum, and W. G. Flannelly, 'Holometrics: An Information Transformation Methodology', *American Helicopter Society 44th Annual Forum*, Washington D.C., June 16-18, pp. 879-85, 1988.
8. C. T. Gunsallus, 'Rotating System Load Monitoring Using Minimum Fixed System Instrumentation', *American Helicopter Society National Specialist Meeting on Fatigue Methodology*, Scottsdale, Arizona, 3-5 Oct. 1989.
9. B. Gustavson, W. L. Pellum, and E. Robeson, 'Systematic Application of Holometric Synthesis for Cost-Effective Flight Load Monitoring', *American Helicopter Society 49th Annual Forum*, St. Louis, Missouri, pp. 793-812, May 19-21, 1993.
10. D. J. Haas, L. Flitter, and J. Milano, 'Helicopter Flight Data Feature Extraction for Component Load Monitoring', *Journal of Aircraft*, v.33, n.1, pp. 37-45, Jan.-Feb. 1996.
11. D. J. Haas, J. Milano, and L. Flitter, 'Prediction of Helicopter Component Loads Using Neural Networks', *Journal of the American Helicopter Society*, v.40, n.1, pp. 72-82, Jan. 1995.
12. M. E. Hoffman, 'Improving Predictions for Helicopter Usage Monitoring', *Proceedings of the USAF Structural Integrity Program Conference*, San Antonio TX, pp. 743-65, 6-8 Dec. 1994.
13. R. W. Jackson, 'Black Hawk Helicopter Component Fatigue Life Substantiation - Parameter Measurement', *Aeronautical Research Laboratories Technical Note 54*, Apr. 1994.

14. K. M. McCool, L. A. Flitter, and D. J. Haas, 'Development and Flight Test Evaluation of a Rotor System Load Monitoring Technology', *Proceedings of the American Helicopter Society 54th Annual Forum*, Washington D.C., May 20-22, 1998.
15. S. S. Tang and L. J. O'Brien, 'A Novel Method for Fatigue Life Monitoring of Non-Airframe Components', Paper AIAA-91-1088-CP, 32nd Structures, Structural Dynamics and Materials Conference, Baltimore, MD, April 1991.
16. S. S. Tang and J. Moffatt, 'Flight Load Models for the On-Board Fatigue Usage Processing of Mechanical Components on Helicopters', *AIAA Dynamics Specialists Conference*, Hilton Head, SC, Paper: AIAA-94-1718, pp. 355-66, 21-22 April, 1994.
17. S. S. Tang and J. Moffatt, 'Development of an On-Board Fatigue Processor for Helicopters', *International Journal of Fatigue*, v.18, n.3, pp. 179-89, 1996.
18. A. M. Leahy, 'Helicopter Fatigue Monitoring—The Way Ahead', *Aerotech Conference*, Oct. 1993.
19. G. L. Barndt and S. Moon, 'Development of a Fatigue Tracking Program for Navy Rotary Wing Aircraft', *Proceedings of the American Helicopter Society 50th Annual Forum*, Washington D.C., pp. 1359-89, May 11-13, 1997.
20. K. F. Fraser, 'General Requirement and Techniques for Component Fatigue Life Substantiation in Australian Service Helicopters', *Aeronautical Research Laboratories Propulsion Report 187*, AR-006-619, Jun. 1991.
21. K. F. Fraser, 'A Review of Life Substantiation and HUMS for Military Helicopters', *Aeronautical and Maritime Research Laboratories (AED)*, DSTO-TASK-0001, Aug. 1994.
22. K. F. Fraser, 'An Overview of Health and Usage Monitoring Systems (HUMS) for Military Helicopters', *Aeronautical and Maritime Research Laboratories (AED)*, DSTO-TR-0061, Sep. 1994.
23. K. F. Fraser, 'Helicopter Life Substantiation: Review of some USA and UK Initiatives', *Aeronautical and Maritime Research Laboratories (AED)*, DSTO-TR-0062, Sep. 1994.
24. L. Krake, 'A Review of the Fatigue Life Substantiation Methodology for Model UH-1D Iroquois Helicopter Dynamic Components', *Aeronautical and Maritime Research Laboratories (AED)*, DSTO-TN-0029, Nov. 1995.
25. D. C. Lombardo, 'Helicopter Structures—A Review of Loads, Fatigue Design Techniques and Usage Monitoring', *Aeronautical Research Laboratories Technical Report 15*, AR-00-137, May 1993.
26. R. Boorla and K. Rotenberger, 'Load Variability of a Two-Bladed Helicopter', *Journal of the American Helicopter Society*, v.42, n.1, pp. 15-26, Jan. 1997.
27. C. G. Schaefer, Jr., 'The Effects of Aerial Combat on Helicopter Structural Integrity', *Proceedings of the American Helicopter Society 45th Annual Forum*, Boston MA, pp. 197-210, 1989.

28. D. J. Haas and R. Imber, 'Identification of Helicopter Component Loads Using Multiple Regression', *Journal of Aircraft*, v.31, n.4, Jul.-Aug. 1994.
29. D. J. Haas, 'Determination of Helicopter Flight Loads from Fixed System Measurements', *Proceedings of the AIAA/ASME/ASCE/AHS/ASC 32nd Structures, Structural Dynamics, and Materials Conference*, Baltimore MD, AIAA, pp. 710-18, 1991.
30. F. G. Polanco, 'A Review of Helicopter Fatigue Prediction Methods', *Aeronautical and Maritime Research Laboratories (AED)*, DSTO series report to be published.
31. E. F. Bruhn, *Analysis and Design of Flight Vehicle Structures*, Jacobs, 1973.
32. S. P. Timoshenko and J. M. Gere, *Theory of Elastic Stability*, McGraw-Hill, 1961.
33. G. H. Golub and C. F. van Loan, *Matrix Computations*, 2nd edn, Johns Hopkins, 1989.
34. S. Wolfram, *The Mathematica Book*, 3rd edn, 1996.
35. W. H. Press, S. A. Teukolsky, W. T. Vetterling, and B. P. Flannery, *Numerical Recipes in C: The Art of Scientific Computing*, 2nd edn, Cambridge, 1992.
36. D. P. Mondkar and G. H. Powell, 'Finite Element Analysis of Non-Linear Static and Dynamic Response', *International Journal for Numerical Methods in Engineering*, v.11, pp. 499-520, 1977.
37. W. C. Young, *Roark's Formulas for Stress and Strain*, 6th edn, McGraw-Hill, 1989.
38. L. Meirovitch, *Elements of Vibration Analysis*, 2nd edn, McGraw-Hill, 1986.
39. A. P. Prudnikov, Yu. A. Brychkov, O. I. Marichev, *Integrals and Series. Volume 1: Elementary Functions*, Gordon and Breach, 1988.

A. Statically Indeterminate Structures Remain Linear

In this appendix we demonstrate two sets of examples showing that statically indeterminate structures have additional complexity (compatibility equations have to be additionally solved), but the problem remains linear. In fact the system will remain linear unless it experiences buckling, large strains (that is, geometric non-linearity), or the material behaviour is non-linear [36, 37].

The two conditions shown in Figure A.1 demonstrate how redundantly constrained structures may be thought of as determinate structures that are pre-stressed. Thus for stress relationships between different members of a truss system, these types of redundancies merely change the constants in the linear system of equations.

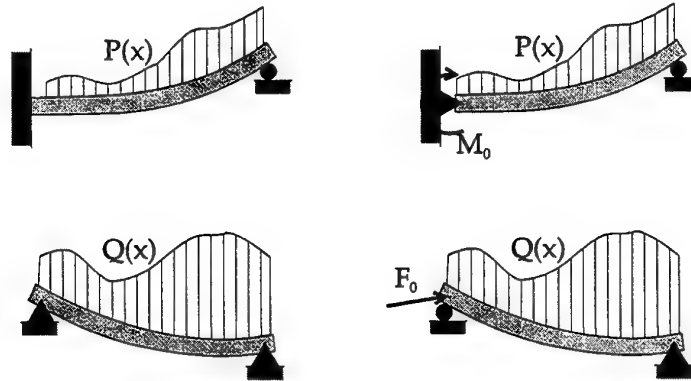


Figure A.1. Some redundant structures (shown on the left) may be thought of as determinate but pre-stressed structures (shown on the right).

Figure A.2 shows a truss system with a redundant member and a vertical and horizontal force at the joint labelled A (all joints are pinned). Using indeterminate truss analysis the forces in the members AD, AB, and AC are given respectively by

$$R_{AD} = \frac{-\sqrt{5}}{2} \left(F_y + \frac{1}{\sqrt{2}} R_{AC} \right),$$

$$R_{AB} = F_x + \frac{1}{2} F_y - \frac{1}{2\sqrt{2}} R_{AC},$$

and

$$R_{AC} = \frac{\sqrt{2} [2c_{AB}F_x + (c_{AB} - 5\sqrt{5}c_{AD})F_y]}{c_{AB} + 8\sqrt{2}c_{AC} + 5\sqrt{5}c_{AD}},$$

where $1/c_{AC}$ is equal to the product of area and Young's modulus for the member AC, that is $c_{AC} = 1/(A_{AC} E_{AC})$ (a similar notation holds for the other members). The last equation was derived using the compatibility equation $\epsilon_{AC} = (\epsilon_{AB} + 5\epsilon_{AD})/4$, where ϵ_{AC} is the strain of the member AC. This simple example demonstrates that the stresses in these members are still linear functions of the external forces F_x and F_y , and thus there is a linear relation between stresses in the truss members. So that if we assume the same Young's modulus for all three member, then the tensile stress in member AC, for example, in terms of the stresses in members AB and AD is

$$\sigma_{AC} = \frac{1}{4}(\sigma_{AB} + 5\sigma_{AD}),$$

where σ_{AB} , σ_{AC} , σ_{AD} , A_{AB} , A_{AC} , and A_{AD} are the tensile stresses and the areas in members AB, AC, and AD respectively.

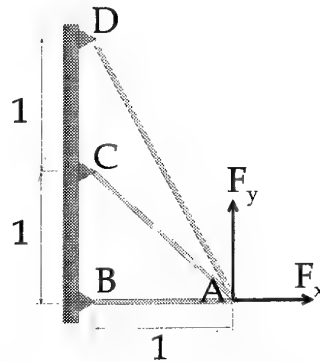


Figure A.2. Even with a redundant member the truss system is still linear.

B.1 Main Rotor Loads on Cabin Section

In this subsection we determine forces and moments (and some shearing forces) on the cabin section of the helicopter (beams AB , AC , BC , and DE) from main rotor loads only (that is, P_x , P_y , and P_m).

The constraint reactions from the ground on pin A and on roller B are respectively

$$R_{Ax} = -P_x, \quad (B.1)$$

$$R_{Ay} = -R_{By} - P_y, \quad (B.2)$$

and

$$R_{By} = (P_x y_E - P_y x_D - P_m) / x_B. \quad (B.3)$$

Separating member DE from the truss and considering its constraining forces gives

$$R_{Cx} = (P_m - P_x y_E) / y_C,$$

$$R_{Dx} = -P_x - R_{Cx},$$

and

$$R_{Dy} = -P_y.$$

In addition to tensile or compressive forces, beams AB and DE (and hence gauges G_0 , G_2 , and G_4) also have bending moments and shear forces. (Shear forces at the strain gauges are not shown below since these forces do not influence gauge readings.) The two angles θ_{DAC} and θ_{DBC} may be written down in terms of lengths yielding

$$\theta_{DAC} = \tan^{-1}(y_C / x_D) \quad \text{and} \quad \theta_{DBC} = \tan^{-1}[y_C / (x_B - x_D)].$$

Then the forces in members AB , AC , BC , and DE are respectively

$$F_{AC} = -F_{BC} \sin \theta_{DBC} / \sin \theta_{DAC},$$

$$F_{BC} = R_{Cx} \sin \theta_{DAC} / \sin(\theta_{DAC} + \theta_{DBC}),$$

$$F_{ADx} = -F_{AC} \cos \theta_{DAC} - R_{Ax},$$

$$F_{ADy} = -F_{AC} \sin \theta_{DAC} - R_{Ay},$$

$$F_{BDx} = -F_{BC} \cos \theta_{DBC},$$

and

$$F_{BDy} = R_{By} + F_{BC} \sin \theta_{DBC},$$

where the forces F_{ADy} and F_{BDy} are shear forces (positive up).

The forces at the gauges may be similarly calculated to give tensile forces (subscript T) and bending moments (subscript M), where the subscript number denotes the corresponding strain gauge. So, for example, F_{T4} represents the tensile force at gauge G_4 , while F_{M0} denotes the (anti-clockwise) bending moment at gauge G_0 . The forces and moments at the strain gauges, due to the main rotor loads, are then

$$F_{T0} = P_y, \quad F_{M0} = P_x(y_E - y_0) + R_{Cx}(y_C - y_0) - P_m, \quad (B.4)$$

$$F_{T1} = F_{AC}, \quad F_{M1} = 0, \quad (B.5)$$

$$F_{T2} = F_{BDx}, \quad F_{M2} = -F_{BDy}(x_B - x_2), \quad (B.6)$$

$$F_{T3} = F_{BC}, \quad F_{M3} = 0, \quad (B.7)$$

$$F_{T4} = F_{ADx}, \quad F_{M4} = -F_{ADy}x_4, \quad (B.8)$$

and

$$F_{T5} = 0, \quad F_{M5} = 0. \quad (B.9)$$

B.2 Accelerations on Cabin Section

The loads and moments on the cabin section arising from mass accelerations are given in this section. The ground constraints resulting from the acceleration of mass m_{AD} are denoted by hatted variables ($\hat{}$), and similarly constraints resulting from mass m_{AC} are denoted by tilded variables ($\tilde{}$). The m_{AD} and m_{AC} resulting reaction forces are given respectively by

$$\hat{R}_{Ax} = -m_{AD}g_x,$$

$$\hat{R}_{Ay} = -\hat{R}_{By} - m_{AD}g_y,$$

$$\hat{R}_{By} = -m_{AD}g_y(x_{Mad}/x_B),$$

and

$$\tilde{R}_{Ax} = -m_{AC}g_x,$$

$$\tilde{R}_{Ay} = -\tilde{R}_{By} - m_{AC}g_y,$$

$$\tilde{R}_{By} = m_{AC} (g_x \sin \theta_{DAC} - g_y \cos \theta_{DAC}) \left(\frac{x_{Mac}}{x_B \cos \theta_{DAC}} \right),$$

where x_{Mac} is the x -coordinate of the point mass m_{AD} . Member forces easily follow giving

$$\tilde{F}_{AB} = -\tilde{F}_{BC} \cos \theta_{DBC},$$

and

$$\tilde{F}_{BC} = -\tilde{R}_{By} / \sin \theta_{DBC}.$$

The strain gauge forces due the combined masses, which we denoted by hatted tilde ($\hat{\sim}$) variables, are

$$\hat{\tilde{F}}_{T0} = 0, \quad \hat{\tilde{F}}_{M0} = 0, \quad (B.10)$$

$$\hat{\tilde{F}}_{T1} = \tilde{F}_{BC} \cos(\theta_{DAC} + \theta_{DBC}), \quad \hat{\tilde{F}}_{M1} = \tilde{F}_{BC} \sin(\theta_{DAC} + \theta_{DBC}) \left(\frac{x_C - x_1}{\cos \theta_{DAC}} \right), \quad (B.11)$$

$$\hat{\tilde{F}}_{T2} = \tilde{F}_{AB}, \quad \hat{\tilde{F}}_{M2} = -\hat{R}_{By} (x_B - x_2), \quad (B.12)$$

$$\hat{\tilde{F}}_{T3} = \tilde{F}_{BC}, \quad \hat{\tilde{F}}_{M3} = 0, \quad (B.13)$$

$$\hat{\tilde{F}}_{T4} = \tilde{F}_{AB}, \quad \hat{\tilde{F}}_{M4} = -\hat{R}_{By} (x_B - x_4), \quad (B.14)$$

and

$$\hat{\tilde{F}}_{T5} = 0, \quad \hat{\tilde{F}}_{M5} = 0. \quad (B.15)$$

B.3 Tail Loads

All reactions to tail loads have a dashed (') notation. Considering tail rotor loads only, the constraint reactions from the ground on pin A and on roller B are respectively

$$R'_{Ax} = -T_x,$$

$$R'_{Ay} = -T_y - R'_{By},$$

and

$$R'_{By} = -T_y + F'_{CH} [y_C \cos \theta_{CHXX} - (x_B - x_C) \sin \theta_{CHXX}] / x_B,$$

where $\theta_{CHXX} = \tan^{-1}[(y_C - y_H)/(x_H - x_C)]$ is the angle made by the member CH with the horizontal (denoted by XX) and F'_{CH} is defined below. To help with the derivation of member forces F_{BG} and F_{BH} below note that the geometric ratios y_C/x_B and $(x_B - x_C)/x_B$ in the expression for R'_{By} shown above have the equivalent trigonometric forms

$$y_C/x_B = \tan \theta_{DAC} \tan \theta_{DBC} / (\tan \theta_{DAC} + \tan \theta_{DBC})$$

and

$$(x_B - x_C)/x_B = \tan \theta_{DAC} / (\tan \theta_{DAC} + \tan \theta_{DBC}).$$

The member forces are

$$F'_{CH} = \frac{T_x y_F - T_y (x_F - x_B) - T_m}{y_H \cos \theta_{CHXX} + (x_H - x_B) \sin \theta_{CHXX}},$$

$$F'_{AC} = \frac{F'_{CH} (\cos \theta_{CHXX} \tan \theta_{DBC} - \sin \theta_{CHXX})}{\sin \theta_{DAC} + \cos \theta_{DAC} \tan \theta_{DBC}},$$

$$F'_{BC} = \frac{-F'_{CH} \cos \theta_{CHXX} + F'_{AC} \cos \theta_{DAC}}{\cos \theta_{DBC}},$$

$$F'_{BG} = \frac{T_y - T_x \tan \theta_{BHXX} + F'_{CH} \cos \theta_{CHXX} (\tan \theta_{BHXX} + \tan \theta_{CHXX})}{\cos \theta_{BGXX} (\tan \theta_{BGXX} - \tan \theta_{BHXX})},$$

$$F'_{BH} = \frac{T_y - T_x \tan \theta_{BGXX} + F'_{CH} \cos \theta_{CHXX} (\tan \theta_{BGXX} + \tan \theta_{CHXX})}{\cos \theta_{BHXX} (\tan \theta_{BHXX} - \tan \theta_{BGXX})},$$

and

$$F'_{AB} = -F'_{AC} \cos \theta_{DAC} - R'_{Ax}.$$

And thus the gauge moments and tensile forces are

$$F'_{T0} = 0, \quad F'_{M0} = 0, \quad (B.16)$$

$$F'_{T1} = F'_{AC}, \quad F'_{M1} = 0, \quad (B.17)$$

$$F'_{T2} = F'_{AB}, \quad F'_{M2} = 0, \quad (B.18)$$

$$F'_{T3} = F'_{BC}, \quad F'_{M3} = 0, \quad (B.19)$$

$$F'_{T4} = F'_{AB}, \quad F'_{M4} = 0, \quad (B.20)$$

$$F'_{T5} = F'_{CH}, \quad F'_{M5} = 0, \quad (B.21)$$

$$F'_{T6} = F'_{BH}, \quad F'_{M6} = 0, \quad (B.22)$$

and

$$F'_{T7} = F'_{BG}, \quad F'_{M7} = 0. \quad (B.23)$$

B.4 Stresses at Strain Gauge Locations

Now that we have all the member tensile forces and moments under the loading shown in Figure B.1 we can simply state the stresses at the strain gauge locations. Tensile forces F will cause a tensile stress σ given by the relation $\sigma = F/A$, where A is the beam's cross sectional area at the strain gauge location. Similarly the bending moment F_M will cause a stress σ given by $\sigma = F_M r/I$, where I is the beam's second moment of area at the strain gauge location and r is the distance from the neutral axis to the gauge-beam contact surface. We then have in general that the stress at the j th strain gauge is

$$\sigma_j = \frac{1}{A_j} \left(F_j + \hat{F}_j + F'_j \right) + \frac{r_j}{I_j} \left(F_{Mj} + \hat{F}_{Mj} + F'_{Mj} \right),$$

where A_j is the cross sectional area, r_j is the distance from the neutral axis to the strain gauge, and I_j is the second moment of area at the j th strain gauge location. (The sign in front of the moments F_{Mj} , \hat{F}_{Mj} , and F'_{Mj} is positive if the j th strain gauge is in tension under that moment and negative otherwise.) More concretely we have that

$$\sigma_0 = \frac{P_y}{A_0} + \frac{r_0}{I_0} [P_x (y_E - y_0) + R_{Cx} (y_C - y_0) - P_m],$$

$$\sigma_1 = \frac{1}{A_1} [F_{AC} + \tilde{F}_{BC} \cos(\theta_{DAC} + \theta_{DBC}) + F'_{AC}] + \frac{r_1}{I_1} \tilde{F}_{BC} \left(\frac{x_C - x_1}{\cos \theta_{DAC}} \right) \sin(\theta_{DAC} + \theta_{DBC}),$$

$$\sigma_2 = \frac{1}{A_2} (F_{BDx} + \tilde{F}_{AB} + F'_{AB}) + \frac{r_2}{I_2} (-F_{BDy} - \hat{R}_{By})(x_B - x_2),$$

$$\sigma_3 = \frac{1}{A_3} (F_{BC} + \tilde{F}_{BC} + F'_{BC}),$$

$$\sigma_4 = \frac{1}{A_4} (F_{ADx} + \tilde{F}_{AB} + F'_{AB}) + \frac{r_4}{I_4} [-F_{ADy} x_4 - \hat{R}_{By} (x_B - x_4)],$$

$$\sigma_5 = \frac{F'_{CH}}{A_5}, \quad \sigma_6 = \frac{F'_{BH}}{A_6}, \quad \text{and} \quad \sigma_7 = \frac{F'_{BG}}{A_7},$$

where beam forces and ground reactions are given by Equations (B.1)–(B.23).

The stress equations shown above were verified numerically using NASTRAN, the results are shown in Table B.1. The last column gives a numerical comparison between the analytic results and the NASTRAN model in terms of relative error, defined as (NASTRAN-analytic)/analytic. The input loading for this comparison was arbitrarily chosen to be $P_x=7$, $P_y=8$, and $P_m=9$ for the main rotor, $T_x=3$, $T_y=1$, and $T_m=13$ for the tail rotor, and $g_x=5$ and $g_y=6$ for the accelerations (or inertial loads as termed in NASTRAN). As can be seen the derived stresses compare well with the NASTRAN model. For some reason the stress recovery at strain gauge G_0 gave the incorrect result -6.7528×10^6 . However, the correct result is shown in Table B.1 derived from NASTRAN's beam axial force and bending moment at strain gauge G_0 . Increasing the number of elements by a factor of four (by twice splitting each element in half) eliminated this NASTRAN self-inconsistency between the recovered stress and the axial force and bending moment at gauge G_0 .

Strain Gauge	Analytic	NASTRAN	Relative Error
0	-1.2725×10^6	$-1.2725 \times 10^{6\dagger}$	-2.3477×10^{-6}
1	3.6824×10^6	3.6824×10^6	3.5439×10^{-8}
2	2.9202×10^6	2.9202×10^6	1.7874×10^{-6}
3	3.9764×10^4	3.9771×10^4	-1.7304×10^{-4}
4	6.8519×10^6	6.8519×10^6	1.2394×10^{-6}
5	-4.1779×10^4	-4.1780×10^4	-1.8601×10^{-5}
6	-7.8983×10^4	-7.8983×10^4	-3.6965×10^{-7}
7	1.0504×10^5	1.0504×10^5	-4.1463×10^{-7}

Table B.1 Comparison between the analytic results and a NASTRAN model.

Joint	A	B	C	D	E	F	G	H
Point	1	2	3	4	5	6	7	8
x	0.0	3.0	2.0	2.0	2.0	7.5	3.6	3.3
y	0.0	0.0	1.0	0.0	1.5	0.8	0.6	0.9

Table B.2 Location of NASTRAN truss model joints.

[†] This value was derived using the NASTRAN's beam axial force and bending moment instead of the NASTRAN's beam stress recovery option, which was used for all the other strain gauges. See main text for further details.

Line	1	2	3	4	5	6	7	8	9	10
Point 1	1	1	4	2	2	2	8	8	8	7
Point 2	2	3	5	3	7	8	3	7	6	6
Num. of Elements	6	4	3	3	2	2	3	1	8	7

Table B.3 Number of elements in each beam for the NASTRAN truss model.

The NASTRAN model used beam (BAR2) elements that were pinned using multi-point constraints. The x - and y -coordinates of the truss' joints are shown in Table B.2, while Table B.3 shows the number of elements in each beam. All beams had the same, circular tube cross-section (of inner radius 0.015 and thickness 0.005), Poisson ratio ($\nu=0.3$), and Young's modulus ($E=200 \times 10^9$). The two point masses were $m_{AC}=9$ and $m_{AD}=7$.

C. Effect of Vibration on Static Assumption

In this appendix we determine under what conditions the assumption of negligible vibration leads to grossly inaccurate results. We begin by investigating the dynamic properties of a simple beam pinned at both ends, as shown in Figure C.1, under a transverse dynamic loading.

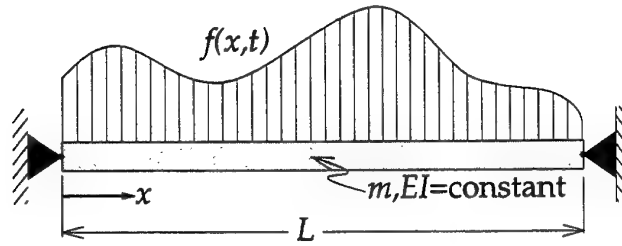


Figure C.1. Transverse vibration of a pinned beam with constant mass and stiffness.

The beam shown above is governed by the following partial differential equation [38, p. 222]

$$m \frac{\partial^2 y}{\partial t^2} + EI \frac{\partial^4 y}{\partial x^4} = f(x, t), \quad 0 < x < L,$$

where $y(x, t)$ is the vertical displacement at time t and at a point x along the beam, m and EI are the mass and stiffness (both constant) of the beam, and $f(x, t)$ is the loading distribution as a function of space and time. Consider the initial conditions

$$y(x, 0) = y_0(x) \quad (\text{initial displacement}),$$

$$\left. \frac{\partial y}{\partial t} \right|_{t=0} = v_0(x) \quad (\text{initial velocity}),$$

and boundary conditions

$$\begin{aligned} y(0, t) &= 0, & EI \frac{\partial^2 y}{\partial x^2} \bigg|_{x=0} &= 0, \\ y(L, t) &= 0, & EI \frac{\partial^2 y}{\partial x^2} \bigg|_{x=L} &= 0, \end{aligned}$$

where the second condition on both lines is equivalent to a zero bending moment since $M = EI \partial^2 y / \partial x^2$. The solution for transverse vibration of the beam shown in Figure C.1 under the above initial and boundary conditions is given by Meirovitch [38, pp. 235-37] as

$$y(x, t) = \sum_{n=1}^{\infty} Y_n(x) \left\{ \frac{1}{\omega_n} \int_0^t Q_n(\tau) \sin[\omega_n(t - \tau)] d\tau + q_{n_0} \cos(\omega_n t) + \frac{\dot{q}_{n_0}}{\omega_n} \sin(\omega_n t) \right\},$$

where the natural frequencies and modes are given respectively by

$$\omega_n = \left(\frac{n\pi}{L} \right)^2 \sqrt{\frac{EI}{m}},$$

and

$$Y_n(x) = \sqrt{\frac{2}{mL}} \sin\left(\frac{n\pi x}{L}\right),$$

and the generalised forces, coordinates, and velocities are given respectively by

$$Q_n(t) = \int_0^L f(x, t) Y_n(x) dx,$$

$$q_{n_0} = \int_0^L m y_0(x) Y_n(x) dx,$$

and

$$\dot{q}_{n_0} = \int_0^L m v_0(x) Y_n(x) dx.$$

We want to determine how the stress response of a beam varies as the forcing frequency approaches the first natural frequency of the beam. Under a static force F applied at a point $x = \alpha L$ along the beam, where $\alpha \in (0, 1)$, the static stress is given by Young [37, p. 100] as

$$\sigma_{\text{stat}} = \frac{Fz}{I} [(1 - \alpha)x - (x - \alpha L)h(x - \alpha L)],$$

where z is the distance from the neutral axis to the fibre at which stress is to be measured (usually the extreme fibre), x is measured from the left end of the beam, I is the moment of inertia with respect to the neutral axis, and $h(x - \alpha L)$ is a step function such that $h(x - \alpha L) = 0$ if $x < \alpha L$ and $h(x - \alpha L) = 1$ if $x > \alpha L$.

We want to compare the above static solution with that of a cyclically applied load and corresponding vibratory response. Assume the distributed loading shown in Figure C.1 is given by

$$f(x, t) = -F \delta(x - \alpha L) \sin(\omega_F t + \theta_F),$$

where $\delta(x - \alpha L)$ is the delta function defined such that $\int_{\tau-\varepsilon}^{\tau+\varepsilon} \delta(x - \tau) f(x) dx = f(\tau)$ for any $\varepsilon > 0$. Thus the above forcing function represents a cyclic point force at $x = \alpha L$ having a maximum force F , angular frequency ω_F , and phase shift θ_F .

For simplicity we consider the case of zero initial conditions, $y_0(x) = v_0(x) = 0$, and a zero phase shift $\theta_F = 0$ which yields the solution

$$y(x, t) = -\frac{F}{I} \left(\frac{2L^3}{\pi^4 E} \right) \sum_{n=1}^{\infty} \frac{\sin(n\pi\alpha) \sin(n\pi x/L)}{n^4 - \beta_1^2} \phi_n(t)$$

where

$$\phi_n(t) = \sin(\omega_F t) - \frac{\beta_1}{n^2} \sin\left(\frac{n^2}{\beta_1} \omega_F t\right)$$

and $\beta_1 = \omega_F / \omega_1$ is the ratio of the forcing frequency to the first natural frequency. So that as β_1 tends to zero the forcing is slow when compared to the unforced vibration of the beam, while when β_1 tends to unity the forcing frequency is close to the first natural frequency.

The relation between stress and bending moment is $\sigma = Mz/I$, while $M = EI \partial^2 y / \partial x^2$ gives the relation between bending moment and displacement. Thus twice differentiating the displacement, given above, yields the dynamic stress

$$\sigma_{\text{dyn}} = \frac{Fz}{I} \left(\frac{2L}{\pi^2} \right) \sum_{n=1}^{\infty} \left[\frac{\phi_n(t)}{1 - (\beta_1/n^2)^2} \right] \frac{\sin(n\pi\alpha) \sin(n\pi x/L)}{n^2}.$$

The series above can easily be shown to be convergent. Clearly the expression after the summation symbol in the above series is less than $2/n^2$, in modulus, for n sufficiently large. And since the $\sum 2/n^2$ is absolutely convergent, then the series in the expression of dynamic stress is also absolutely convergent. Thus we may re-arrange the summation of the series as follows.

We expect the series to be dominated by the first term, so we separate the first term out giving

$$\sigma_{\text{dyn}} = \frac{Fz}{I} \left(\frac{2L}{\pi^2} \right) \left\{ \sin(\omega_F t) \left[\frac{\sin(\pi\alpha)\sin(\pi x/L)}{(1-\beta_1^2)} + \sum_{n=2}^{\infty} \frac{1}{[1-(\beta_1/n^2)^2]} \frac{\sin(n\pi\alpha)\sin(n\pi x/L)}{n^2} \right] \right. \\ \left. - \beta_1 \left[\frac{\sin(\omega_F t/\beta_1)}{(1-\beta_1^2)} \sin(\pi\alpha)\sin(\pi x/L) + \sum_{n=2}^{\infty} \frac{\sin(\omega_F t n^2/\beta_1)}{[1-(\beta_1/n^2)^2]} \frac{\sin(n\pi\alpha)\sin(n\pi x/L)}{n^4} \right] \right\}$$

Using Prudnikov [39, p. 743 #4] we know the solution of a series similar to the first series

$$\sum_{n=2}^{\infty} \frac{\sin(n\pi\alpha)\sin(n\pi x/L)}{n^2} = -\sin(\pi\alpha)\sin(\pi x/L) + \frac{\pi^2}{2L} [(1-\alpha)x - (x-\alpha L)h(x-\alpha L)],$$

and we can approximately bound the second series by

$$\left| \sum_{n=2}^{\infty} \frac{\sin(\omega_F t n^2/\beta_1)}{[1-(\beta_1/n^2)^2]} \frac{\sin(n\pi\alpha)\sin(n\pi x/L)}{n^4} \right| \lesssim \sum_{n=2}^{\infty} \frac{1}{n^4} = \frac{\pi^4}{90} - 1.$$

This is only an approximate bound because the term $1 - (\beta_1/n^2)^2$ is less than unity. But since $\beta_1 < 1$ this term rapidly approaches unity as n increases, and hence the above bound is an excellent approximation to the true bound. The same argument applies to the first series. In fact, the modulus of the series shown above has the exact bound $(\pi^4/90 - 1)/|1 - \beta_1/16|$.

Using the above two relations we may approximate the dynamic stress by

$$\sigma_{\text{dyn}} \approx \frac{Fz}{I} \left(\frac{2L}{\pi^2} \right) \left\{ \sin(\omega_F t) \left[\sin(\pi\alpha)\sin(\pi x/L) \left(\frac{1}{(1-\beta_1^2)} - 1 \right) + \frac{\pi^2}{2L} [(1-\alpha)x - (x-\alpha L)h(x-\alpha L)] \right] \right. \\ \left. - \beta_1 \left[\frac{\sin(\omega_F t/\beta_1)}{(1-\beta_1^2)} \sin(\pi\alpha)\sin(\pi x/L) + c_1 \left(\frac{\pi^4}{90} - 1 \right) \right] \right\},$$

where $c_1 \in [-1, 1]$. Rewriting the above expression in terms of the static stress and setting c_1 to zero (see discussion below) we obtain

$$\sigma_{\text{dyn}} \approx \sigma_{\text{stat}} [\sin(\omega_F t) + g_1(\alpha, x/L) g_2(\beta_1, \omega_F t)]$$

where

$$g_1(\alpha, x/L) = \left(\frac{2}{\pi^2} \right) \frac{\sin(\pi\alpha)\sin(\pi x/L)}{[(1-\alpha)x/L - (x/L - \alpha)h(x/L - \alpha)]}$$

and

$$g_2(\beta_1, \omega_F t) = \frac{\beta_1}{1 - \beta_1^2} [\beta_1 \sin(\omega_F t) - \sin(\omega_F t / \beta_1)].$$

Surface plots of the functions g_1 and g_2 are shown in Figure C.2 and Figure C.3 respectively. The plot of function g_1 shows that the dynamic stress and static stress are similar when the excitation and reading locations are close together (that is, $x \approx \alpha L$) and most similar when the excitation and the reading location are at either end of the beam.

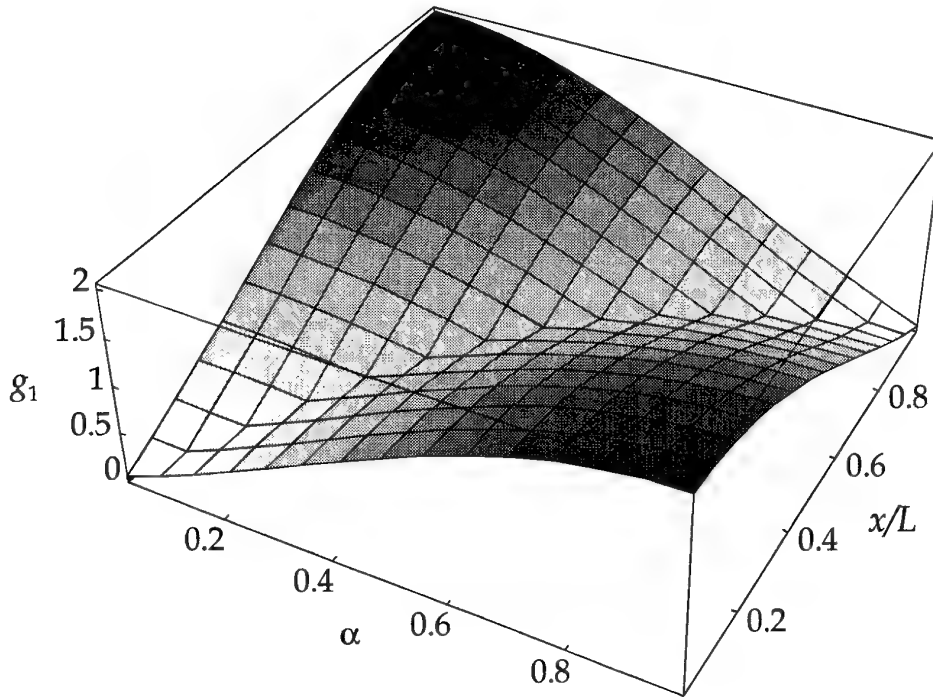


Figure C.2. Function g_1 shows the dynamic stress is very close to the static stress when the excitation and reading location are close together.

Finally by taking the limit of $g_1(\epsilon, \epsilon)$ and $g_1(\epsilon, 1 - \epsilon)$ as ϵ tends to zero yields the lower and upper bounds on function g_1 respectively

$$0 \leq g_1 \leq 2.$$

As expected the plot of the function g_2 shows that the dynamic stress is closest to the static stress when β_1 is small (that is when the loading frequency is much smaller than the first natural frequency). It is easy to show that the function g_2 is bound by

$$-\frac{\beta_1}{1-\beta_1} \leq g_2 \leq \frac{\beta_1}{1-\beta_1},$$

thus we see that resonance results as β_1 approaches unity (again as expected). The other effect to notice in the plot of g_2 is the chirp effect as $\omega_F t$ grows (this chirping effect is shown more clearly in Figure C.4).

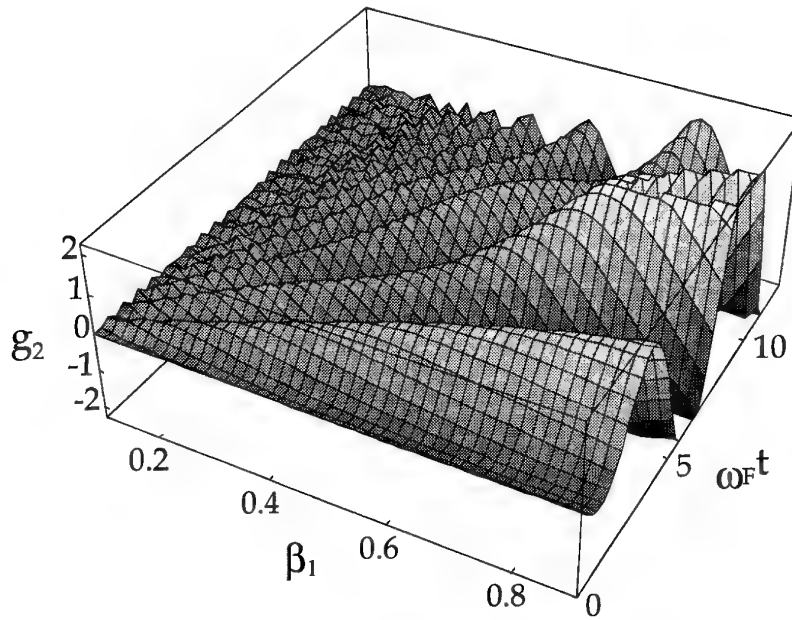


Figure C.3 Function g_2 shows chirping in the β_1 direction as $\omega_F t$ grows.

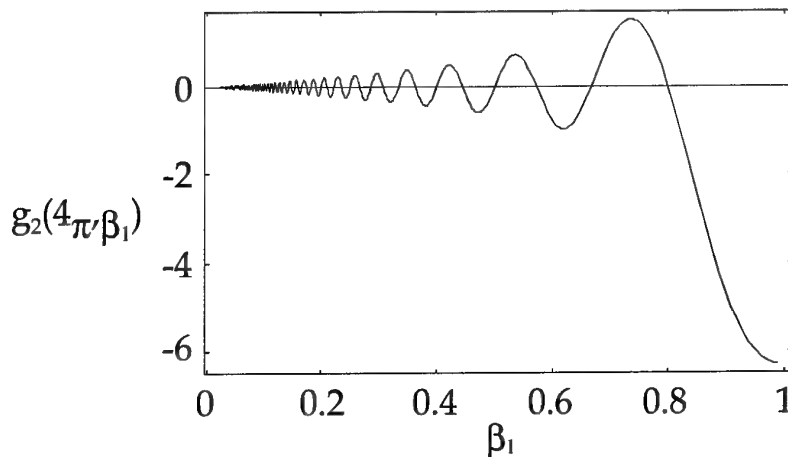


Figure C.4. Chirp effect of the function g_2 evaluated at $\omega_F t = 4\pi$.

Numerical experiments verify that assuming $c_1 = 0$ is a good approximation. To see why let's examine the original series that contained the term $\sin(\omega_F t n^2 / \beta_1)$. For n large we see that this trigonometric function varies rapidly between $[-1, 1]$, and hence acts almost as a random number between these ranges. Thus we would expect that for a large number of cases this would bring the original series close to zero. Setting c_1 to 1 and -1 results in an approximate bound (which may be thought of as an error bound) of the exact solution's approximation.

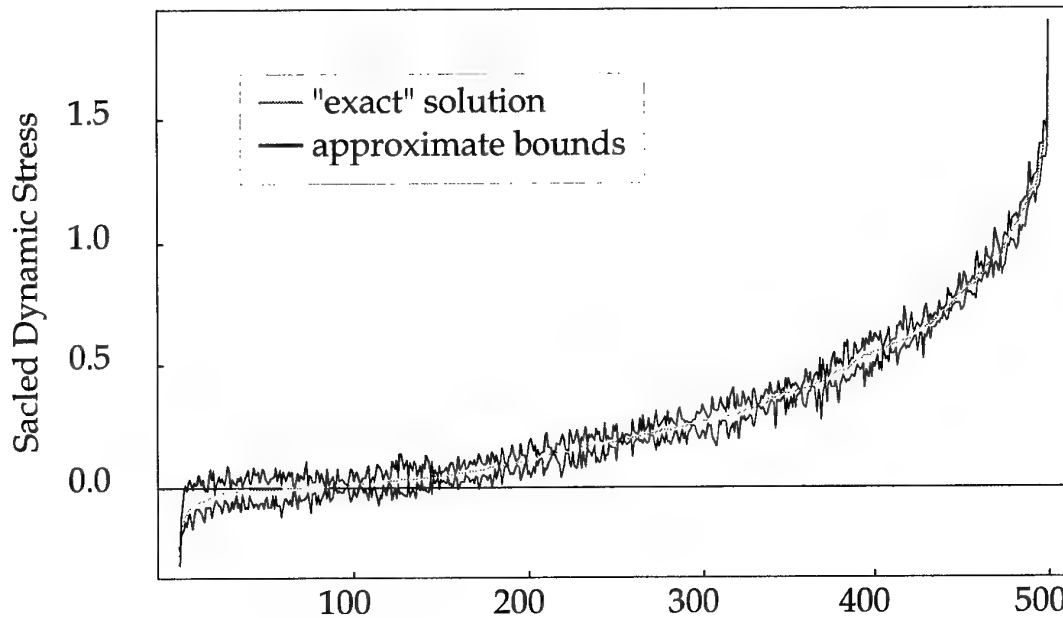


Figure C.5. Comparison of the 'exact' and approximate scaled dynamic stresses for 500 points having randomly distributed arguments. The bounds are determined by setting c_1 to -1 and 1 .

Figure C.5 shows the 'exact' solution, calculated by summing over the first 100 terms of the series, and the upper and lower bounds of the approximate solution. The 500 points were obtained by setting $\omega_F = \pi$ and $L = 1$ and independently randomly distributing β_1 , t , α , and x between $[0, 1]$. For clarity the resulting set of points were sorted by the magnitude of the 'exact' solution and plotted (this explains the smooth monotonic growth of the 'exact' solution of a randomly selected set). As can be seen the upper and lower approximate bounds are extremely accurate. Also the 'exact' solution appears to fall at the mid-point of the upper and lower bounds, justifying the approximation $c_1 = 0$. There was some concern about the accuracy of the approximation as β_1 approached unity, since the series approximations were made assuming $\beta_1 \ll 1$. A plot of the scaled dynamic stress with all variables set to the same values as for Figure C.5, except for $\beta_1 = 0.95$, showed a similar accuracy in the upper and lower bounds for the approximation of dynamic stress as shown in Figure C.5.

Using the two bounds on the functions g_1 and g_2 we arrive at an approximate bound on the difference between the dynamic stress and the static stress as a function of the forcing frequency to the first natural frequency ratio

$$\left| \frac{\sigma_{\text{dyn}}}{\sigma_{\text{stat}}} \right| \approx 1 + \frac{2\beta_1}{1 - \beta_1}.$$

However, if we choose α appropriately, then the bound on function g_1 becomes $0 \leq g_1 \leq 8/\pi^2 \approx 0.8106$, and hence

$$\left| \frac{\sigma_{\text{dyn}}}{\sigma_{\text{stat}}} \right| \lesssim 1 + \frac{0.81\beta_1}{1 - \beta_1} \quad (\text{for appropriately chosen } \alpha).$$

There is a large difference between the dynamic stress and the static stress as the forcing frequency approaches the first natural frequency (the resonance case). Large differences are still noticed away from resonance. For example at $\beta_1 = 0.5$ the dynamic stress can still be as large as three times the equivalent static stress for an inappropriately chosen strain gauge location.

We can draw several conclusions from this simple example comparing the stress of a dynamic response with the equivalent static case. First, if the vibration originates in another part of the truss, then the only way it can enter a beam under consideration is through the ends (assuming end supports). Assuming vibrations are being introduced from both ends, then Figure C.2 suggests the best place for the strain gauge would be in the middle. However, if vibrations are introduced only from one end of the beam, then the best strain gauge location (if only the static component of stress is required) would be at the opposite end of the beam. The above analysis also suggests that the vibration component can only be adequately ignored when either (or both) of the two following conditions is satisfied:

- The forcing frequency is significantly smaller than the first natural frequency, that is $\beta_1 \lesssim 0.048$ (or $\beta_1 \lesssim 0.075$ if α is appropriately chosen). (This choice of β_1 yields a maximum error of 10% in making a static assumption for dynamic loading).
- The forcing amplitude is smaller than the static loading and the forcing frequency is smaller than the first natural frequency.

D. Least Squares Solutions

In this appendix we review some least squares and singular value decomposition theory.

D.1 Singular Value Decomposition

Following the outline in Golub and van Loan [33, p. 71], the singular value decomposition (SVD) of a real m -by- n matrix A is

$$U^T A V = D,$$

where the matrix D is diagonal and the matrices U and V are orthogonal, and have the following structure

$$D = \text{diag}(\sigma_1, \dots, \sigma_p) \quad p = \min\{m, n\},$$

$$U = [u_1, \dots, u_m] \in \mathbb{R}^{m \times m},$$

and

$$V = [v_1, \dots, v_n] \in \mathbb{R}^{n \times n}.$$

The function " $\min\{m, n\}$ " means the smaller of m or n . The singular values σ_i are ordered so that $\sigma_1 \geq \sigma_2 \geq \dots \geq \sigma_p \geq 0$. The $\text{span}(u_1, \dots, u_r)$ and $\text{span}(v_{r+1}, \dots, v_n)$ define the range and nullspace of A respectively, where $r = \text{rank}(A)$ (that is, $\sigma_{r+1} = \dots = \sigma_p = 0$). The 2-norm condition number of the matrix A , defined in terms of the singular values, is given by

$$\kappa = \frac{\sigma_1}{\sigma_p},$$

that is, the ratio of the largest to smallest singular values. The 2-norm of the matrix A is simply given by the largest singular value, that is $\|A\|_2 = \sigma_1$. The square of the Frobenius-norm is given by the sum of the singular values squared, that is $\|A\|_F^2 = \sigma_1^2 + \sigma_2^2 + \dots + \sigma_p^2$.

Figure D.1 shows a geometric interpretation of singular values and vectors for the two-dimensional case. The left figure shows the unit circle, which represents all vectors of unit length. While the right figure shows the mapping of the unit circle under the matrix A (a linear transformation). The singular values control the length of the ellipses

axes. In general a singular value decomposition may be thought of as a linear mapping from a hyper-sphere to a hyper-ellipsoid, the singular values controlling the length and the left singular vectors controlling the direction of the hyper-ellipsoid axes. Finally, if the left singular vectors control the hyper-sphere's elongation directions, then the right singular vectors control the remaining transformations of the sphere (for example rotations and reflections). The dashed lines show the effects of the right singular vectors.

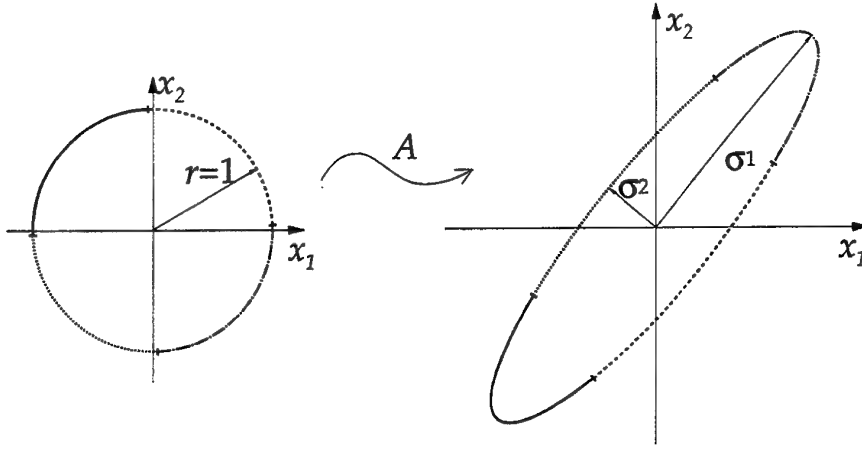


Figure D.1. Illustration of singular values and vectors for the two-dimensional case.

If r is the rank of A then the least squares (LS) solution is given by

$$x_{LS} = \sum_{i=1}^r \frac{u_i^T b}{\sigma_i} v_i = A^+ b$$

where A^+ is the pseudo-inverse (defined below). The solution x_{LS} minimises the 2-norm residual $\|Ax - b\|_2$, and the minimum is given by

$$\|Ax_{LS} - b\|_2^2 = \sum_{i=r+1}^m (u_i^T b)^2.$$

The pseudo-inverse is defined as

$$A^+ = VD^+U^T,$$

where

$$D^+ = \text{diag}\left(\frac{1}{\sigma_1}, \dots, \frac{1}{\sigma_r}, 0, \dots, 0\right) \in \Re^{n \times m}.$$

Golub and van Loan [33] use the pseudo-inverse to show that small changes in A or b can induce arbitrarily large changes in the least squares solution. One approach to determine the numerical rank of A is to assign a tolerance δ such that the singular values are split into two sets

$$\sigma_1 \geq \dots \geq \sigma_r > \delta \geq \sigma_{r+1} \geq \dots \geq \sigma_n,$$

and if the matrix A has sd significant digits one suggested choice for the tolerance is $\delta = 10^{-sd} \|A\|_\infty$.

D.2 Column Weighting

Since the loads that feed into the system are of different natures (for example bending moments, shear forces, and accelerations), the coefficients of the resulting stress equation are most likely to be different orders of magnitude. This variation in magnitude leads to near rank deficient load matrices.

Golub and van Loan [33, p. 251] state that the least squares (LS) solution of the problem

$$\min \|Ax - b\|_2, \quad \text{where } A \in \mathbb{R}^{n \times n} \text{ and } b \in \mathbb{R}^n$$

can be obtained by finding the minimum 2-norm solution y_{LS} to

$$\min \|(AG)y - b\|_2$$

then setting $x_G = Gy_{LS}$, where $G \in \mathbb{R}^{n \times n}$ is non-singular. One choice of G which normalises the columns is

$$G = G_0 = \text{diag}(1/\|A_{:,1}\|_2, \dots, 1/\|A_{:,n}\|_2),$$

where the notation $A_{i,j}$ denotes the i th row and j th column of the matrix A , and thus G_0 transforms each column in A to a unit vector (under a 2-norm). However, since column weighting affects singular values, a scheme for determining numerical rank may not return the same estimates when applied to A and AG .

DSTO-RR-0171

E. Maximum Error of an Approximate Matrix

In this appendix we show that the normalised error of any matrix approximation has two minima and two maxima. Furthermore, the two maxima are of equal magnitude but point in exactly opposite directions, with a similar result holding for the two minima.

Let the matrix \hat{A} be an approximation to a true matrix A . Define the normalised error squared between these two matrices, as a function of some vector x , as

$$\epsilon^2 = \frac{\|\hat{y} - y\|_2^2}{\|y\|_2^2} \quad (E.1)$$

where the vectors y and \hat{y} are the linear transformations of the vector x under the matrices A and \hat{A} respectively (that is $y = Ax$ and $\hat{y} = \hat{A}x$). Defining the error matrix as

$$E = \hat{A} - A,$$

then Equation (E.1) may be re-written as

$$\epsilon^2 = \frac{\|Ex\|_2^2}{\|Ax\|_2^2}. \quad (E.2)$$

Remembering the 2-norm relation $\|z\|_2^2 = z^T \cdot z$ we can easily derive the quadratic form (of $A^T A$)

$$\begin{aligned} \|Ax\|_2^2 &= (Ax)^T \cdot (Ax) \\ &= x^T A^T A x. \end{aligned}$$

Thus we see that the normalised error (E.2) will have exactly two maxima and two minima. We now prove this result for the special case of a two-by-two matrix.

Let the matrix A and the error matrix E be two-by-two matrices and x a two-dimensional vector, each containing elements a_{ij} , e_{ij} , and x_i respectively, so that

$$A = \begin{bmatrix} a_{11} & a_{12} \\ a_{21} & a_{22} \end{bmatrix}, \quad E = \begin{bmatrix} e_{11} & e_{12} \\ e_{21} & e_{22} \end{bmatrix}, \quad \text{and} \quad x = \begin{bmatrix} x_1 \\ x_2 \end{bmatrix}.$$

Then the quadratic form becomes

$$\begin{aligned}\|Ax\|_2^2 &= x^T A^T A x \\ &= (a_{11}^2 + a_{21}^2)x_1^2 + 2(a_{11}a_{12} + a_{21}a_{22})x_1x_2 + (a_{12}^2 + a_{22}^2)x_2^2.\end{aligned}$$

Let the vector x be a unit vector, then we may write x in terms of a real parameter θ so that

$$x = [\cos\theta \quad \sin\theta]^T.$$

Note we have not lost any generality in setting x to be a unit vector since we may divide both numerator and denominator of Equation (E.2) by any scalar. Dividing the numerator and denominator of the normalised error (E.2) by the scalar $\|x\|_2$ forces x to be a unit vector. Using the above unit vector definition of x we can write the normalised error in terms of the parameter θ , which gives

$$\varepsilon^2 = \frac{\alpha_0 + \alpha_1 \cos 2\theta + \alpha_2 \sin 2\theta}{\beta_0 + \beta_1 \cos 2\theta + \beta_2 \sin 2\theta}, \quad (E.3)$$

where the constants α_i are a function of the error matrix E only and are given by

$$\alpha_0 = e_{11}^2 + e_{12}^2 + e_{21}^2 + e_{22}^2,$$

$$\alpha_1 = e_{11}^2 - e_{12}^2 + e_{21}^2 - e_{22}^2,$$

and

$$\alpha_2 = 2(e_{11}e_{12} + e_{21}e_{22}).$$

Similar expressions arise for the β_i constants, except the e_{ij} are replaced by a_{ij} .

We want to determine all stationary points of the normalised error given by Equation (E.3), so as to locate the maximum error. We assume that the matrix A has full rank so that the denominator of Equation (E.3) is non-zero. Differentiating the normalised error with respect to θ and equating the result to zero, after a small amount of simplification we are left with the condition

$$\gamma_0 + \gamma_1 \cos 2\theta + \gamma_2 \sin 2\theta = 0, \quad (E.4)$$

where

$$\gamma_0 = \alpha_2\beta_1 - \alpha_1\beta_2, \quad \gamma_1 = \alpha_2\beta_0 - \alpha_0\beta_2, \quad \text{and} \quad \gamma_2 = \alpha_0\beta_1 - \alpha_1\beta_0$$

are constant. We will show later that we need only consider the range $\theta \in [0, \pi)$, so that the above condition has only two roots (one points in the direction of the maximum and the other in the direction of the minimum). The condition for stationary points of the normalised error given by Equation (E.4) can be shown to be a quartic in $\cos 2\theta$ with two roots (that are repeated) given by

$$\cos 2\theta = \frac{-\gamma_0 \gamma_1 \pm \gamma_2 \sqrt{\gamma_1^2 + \gamma_2^2 - \gamma_0^2}}{\gamma_1^2 + \gamma_2^2}.$$

For the denominator in the above expression to be zero, we require that $\gamma_1^2 + \gamma_2^2 = 0$, which implies that $\alpha_0/\beta_0 = \alpha_1/\beta_1 = \alpha_2/\beta_2$. Thus the only way this denominator can be zero is if the matrix E is a scalar multiple of the matrix A , in which case the normalised error is identically equal to that scalar multiple for all values of θ .

Using Equation (E.2) we see that if a vector x maximises the error giving the value ε_{\max} , then the diametrically opposite vector $-x$ must also maximise the error with the same maximum value ε_{\max} . This justifies the earlier restriction of the parameter θ to the range $\theta \in [0, \pi)$. Using the fact that only one maximum occurs for $\theta \in [0, \pi)$ together with the fact that the second maximum is diametrically opposite to this first maximum proves that the normalised error surface between a two-dimensional matrix A and its approximation contains two maxima. A similar result holds true for the two minima of the normalised error surface.

We can generalise the above result for the n -dimensional case by holding $n-2$ variables fixed and using the above result to show that for the two free variables the normalised error function has two minima and two maxima. Any search algorithm then proves the result to hold for all higher dimensions.

Figure 2.1 shows a three-dimensional example for three orthogonal search paths. We begin by choosing an arbitrary great circle on the unit sphere, then determining the maximum error on this great circle. (This initial great circle and corresponding error function, which is drawn as a projection orthogonal to the sphere, are shown in medium-grey.) Note that the maximum was simple to find since, as we proved, the error function on any great circle has only two maxima (of equal magnitude but diametrically opposite on our sphere). Then we draw a second great circle orthogonal to the first great circle and passing through this error maximum. (This second great circle and corresponding error function are shown in light-grey.) We repeat the previous procedure, finding the error maximum on the second great circle. Then draw a third great circle (shown in black) orthogonal to the second great circle and passing through this second error maximum. Continuing in this same manner we eventually arrive at the maximum. A simple inductive argument carries the proof to all higher dimensions.

An alternative proof is to consider only half the sphere. Then if the error line corresponding to all great circles on this hemi-sphere have only one maximum (which we have already proved), the error surface on this hemi-sphere must have only one maximum. Again, a simple inductive proof carries results onto all higher dimensions.

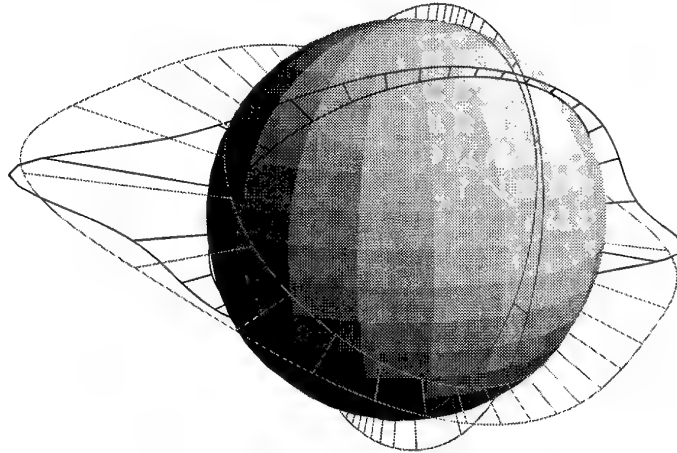


Figure E.1 Three-dimensional visualisation of three search paths (great circles) and their corresponding error functions (drawn as projections emanating orthogonally from the sphere). The first, second, and third search paths are shown in medium-grey, light-grey, and black respectively.

Consideration of the geometric interpretation of singular values (see Appendix D.1) shows that the two maxima for the normalised error must be parallel for the n -dimensional case. If the vector location of one of the maxima is known, then the second maximum is simply given by the same vector in the reverse direction. Figure E.2 illustrates this point for the two-dimensional case.

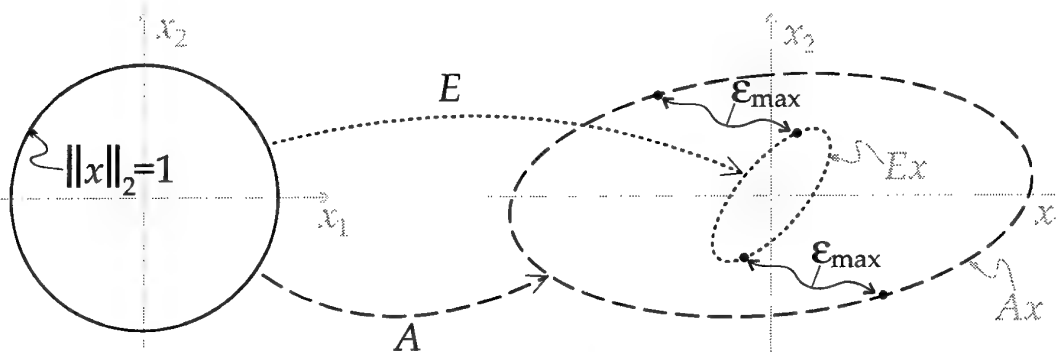


Figure E.2. Linear transformation of unit vectors by the error matrix E and the true matrix A . The maximum normalised errors lie on the same line (radiating from the origin) but in the opposite direction.

Finally, it appears possible that using singular value decomposition information alone the maxima and minima of the error surface could be directly found without resorting to an iterative minimisation or maximisation algorithm. However, this approach was not investigated.

E.1 Regions of Maximum Error

In the preceding section we showed that the maximum error occurred on the n th dimensional hyper-sphere given by the unit force vector, and that the error surface was quartic (with repeated roots). Figure E.3 shows four random examples of the quartic error surface for the two-dimensional case. The inner curve is the unit circle, while the outer curve is the quartic error surface.

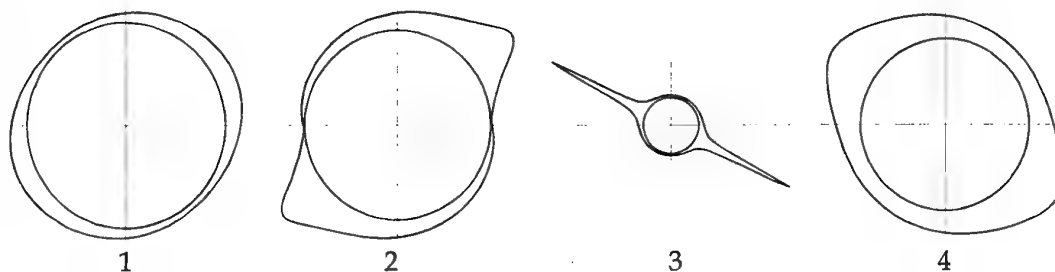


Figure E.3 The error surface corresponding to four random E and A matrices. Ill-conditioned A matrices usually lead to localised errors.

The condition numbers for the error and exact matrices, $\kappa(E)$ and $\kappa(A)$, along with the error bound, $\sigma_{\max}(E)/\sigma_{\min}(A)$, for the four examples in Figure E.3 are shown in Table E.1. We see from this small sample that it is the condition number of the exact matrix A that determines whether or not the maximum error is localised. Thus if the exact matrix is ill-conditioned and the error matrices E are uniformly distributed and not too ill-conditioned, then on the average we can expect localisation of the two maximum error regions.

Example	1	2	3	4
$\kappa(E)$	2.29	52.1	1.55	1.34
$\kappa(A)$	1.70	6.41	54.1	2.97
$\sigma_{\max}(E)/\sigma_{\min}(A)$	0.210	0.968	5.06	0.687

Table E.1 Condition numbers and error for the examples in Figure E.3.

Let us consider several different scenarios for the two-dimensional case to further illuminate the above statements. Assume that, for the matrices E and A , all these scenarios have the same set of singular values (SVs) but different orientations (refer to Figure D.1). That is, in the terminology of Appendix D.1, the SV and right singular vectors remain the same, and only the left singular vectors change between scenarios. Furthermore, so that the matrix A dominates the response of the error surface, assumed the ratio of condition numbers (of A to E) is large, that is $\kappa(A)/\kappa(E) \gg 1$. (This assumption corresponds to A ill-conditioned and E far less ill-conditioned.) Then the two error regions surrounding the two maxima will be most localised when the

orientations of $\sigma_1(E)$ (the largest SV of E) and $\sigma_2(A)$ (smallest SV of A) are collinear. At the other extreme, the two error regions surrounding the two maxima will be most smeared when the orientations of $\sigma_2(E)$ (the smallest SV of E) and $\sigma_2(A)$ (smallest SV of A) are collinear. However, it is the matrix A that dominates the control of the error surface. Hence for most cases it is the amount of ill-conditioning within matrix A that will affect whether or not the region of maximum error is localised. Under the above assumptions, we also expect that these localised error regions will become more pronounced with increasing matrix dimension.

DISTRIBUTION LIST

Development of a Stress Transfer Function for an Idealised Helicopter Structure

F.G. Polanco

AUSTRALIA

DEFENCE ORGANISATION

S&T Program

Chief Defence Scientist	} shared copy
FAS Science Policy	
AS Science Corporate Management	
Director General Science Policy Development	
Counsellor Defence Science, London (Doc Data Sheet)	
Counsellor Defence Science, Washington (Doc Data Sheet)	
Scientific Adviser to MRDC Thailand (Doc Data Sheet)	
Scientific Adviser Policy and Command	
Navy Scientific Adviser (Doc Data Sheet)	
Scientific Adviser - Army (Doc Data Sheet)	
Air Force Scientific Adviser	
Director Trials	

Aeronautical and Maritime Research Laboratory

Director
Chief of Airframes and Engines Division
Research Leader Propulsion
Head Helicopter Life Assessment (K.F. Fraser)
Task Manager (A. Wong)
Author
R.P. Boykett
D.C. Lombardo
C.G. Knight
L. Krake
C. Vavlitis

DSTO Library

Library Fishermans Bend
Library Maribyrnong
Library Salisbury (2 copies)
Australian Archives
Library, MOD, Pyrmont (Doc Data sheet only)
US Defence Technical Information Center, 2 copies
UK Defence Research Information Centre, 2 copies
Canada Defence Scientific Information Service, 1 copy
NZ Defence Information Centre, 1 copy
National Library of Australia, 1 copy

Capability Systems Staff

Director General Maritime Development (Doc Data Sheet only)
Director General C3I Development (Doc Data Sheet only)
Director General Aerospace Development (Doc Data Sheet only)

Navy

Chief Engineer, Naval Aircraft Logistics Management Squadron, HMAS
Albatross, Nowra

Army

ABCA Office, G-1-34, Russell Offices, Canberra (4 copies)
SO (Science), DJFHQ(L), MILPO Enoggera, Queensland 4051 (Doc Data Sheet
only)
Commander Aviation Support Group, Oakey
NAPOC QWG Engineer NBCD c/- DENGRS-A, HQ Engineer Centre Liverpool
Military Area, NSW 2174 (Doc Data Sheet only)

Air Force

Director General Technical Airworthiness (Attn OIC RWS), RAAF Williams
Chief Engineer, Army Aircraft Logistics Management Squadron, Oakey

Intelligence Program

DGSTA Defence Intelligence Organisation
Manager, Information Centre, Defence Intelligence Organisation

Corporate Support Program (libraries)

OIC TRS, Defence Regional Library, Canberra

UNIVERSITIES AND COLLEGES

Australian Defence Force Academy
Library
Head of Aerospace and Mechanical Engineering
Serials Section (M list), Deakin University Library, Geelong Senior Librarian,
Hargrave Library, Monash University (Doc Data Sheet only)
Librarian, Flinders University

OTHER ORGANISATIONS

NASA (Canberra)
AGPS

OUTSIDE AUSTRALIA**ABSTRACTING AND INFORMATION ORGANISATIONS**

Library, Chemical Abstracts Reference Service
Engineering Societies Library, US
Materials Information, Cambridge Scientific Abstracts, US
Documents Librarian, The Center for Research Libraries, US

INFORMATION EXCHANGE AGREEMENT PARTNERS

Acquisitions Unit, Science Reference and Information Service, UK
Library - Exchange Desk, National Institute of Standards and Technology, US

Inderjit Chopra, Minta-Martin Professor and Director, Alfred Gessow Rotorcraft
Center, Aerospace Engineering, University of Maryland, Maryland
Charlie Crawford, Chief Engineer, Aerospace and Transportation Laboratory,
Georgia Tech Research Institute, Alabama
Prof Phil Irving, Head Damage Tolerance Group, School of Industrial and
Manufacturing Science, Cranfield University, Cranfield
Dorothy Holford, Defence Evaluation and Research Agency, Farnborough,
Hampshire

U.S. Army

Eric Robeson, Aviation Applied Technology Directorate, (Fort Eustis, Virginia)
Dr Wolf Elber, Director Vehicle Structures Directorate, NASA Langley Research
Center (Hampton, Virginia)
Kevin Rotenberger, Aviation and Missile Command (Redstone Arsenal,
Alabama)

U.S. Navy

Gene Barndt, Rotary Wing Structures, NAVAIRSYSCOM (Patuxent River,
Maryland)

SPARES (5 copies)

Total number of copies: 67

DEFENCE SCIENCE AND TECHNOLOGY ORGANISATION DOCUMENT CONTROL DATA					
				1. PRIVACY MARKING/CAVEAT (OF DOCUMENT)	
2. TITLE Development of a Stress Transfer Function for an Idealised Helicopter Structure			3. SECURITY CLASSIFICATION (FOR UNCLASSIFIED REPORTS THAT ARE LIMITED RELEASE USE (L) NEXT TO DOCUMENT CLASSIFICATION) Document (U) Title (U) Abstract (U)		
4. AUTHOR(S) Frank G. Polanco			5. CORPORATE AUTHOR Aeronautical and Maritime Research Laboratory PO Box 4331 Melbourne Vic 3001 Australia		
6a. DSTO NUMBER DSTO-RR-0171		6b. AR NUMBER AR-011-237		7. DOCUMENT DATE March 2000	
8. FILE NUMBER M1/9/649		9. TASK NUMBER 98/210		10. TASK SPONSOR DSTO	
				11. NO. OF PAGES 64	
				12. NO. OF REFERENCES 39	
13. URL http://www.dsto.defence.gov.au/corporate/reports/DSTO-RR-0171.pdf			14. RELEASE AUTHORITY Chief, Airframes and Engines Division		
15. SECONDARY RELEASE STATEMENT OF THIS DOCUMENT <i>Approved for public release</i> OVERSEAS ENQUIRIES OUTSIDE STATED LIMITATIONS SHOULD BE REFERRED THROUGH DOCUMENT EXCHANGE CENTRE, DIS NETWORK OFFICE, DEPT OF DEFENCE, CAMPBELL PARK OFFICES, CANBERRA ACT 2600					
16. DELIBERATE ANNOUNCEMENT No Limitations					
17. CASUAL ANNOUNCEMENT Yes					
18. DEFTEST DESCRIPTORS Defence Projects (Australia), aircraft structures, structural analysis, fatigue (materials), spectra, military helicopters, Health and Usage Monitoring Systems					
19. ABSTRACT This report presents an investigation of the effects that may have an influence on the development of a linear stress transfer function (STF) relating the stress in dynamic components to the stress in static components. Effects such as buckling, non-uniqueness, vibration, and solution procedure are considered. Two procedures for determining the STF are compared, one termed the vector procedure and the other the matrix procedure. A simple two dimensional truss, which models an idealised helicopter structure, is constructed to numerically simulate the development of a STF. Using random inputs the resulting stresses are evaluated exactly. Noise is then added to both the input loads and output stresses to develop a noisy data set. Using this noisy data set, STFs are developed using both the vector and matrix techniques. The vector procedure is shown to be sensitive to collinearity in the input, while the matrix technique is found to be more stable under the same ill-conditioning.					